BASS. XXXV. The $M_{\rm BH}$–σ^* Relation of 105 Month Swift-BAT Type 1 AGNs

Turgay Caglar[1] , Michael J. Koss[2,3] , Leonard Burtscher[1] , Benny Trakhtenbrot[4] , M. Kiyami Erdim[5] ,
Julian E. Mejía-Restrepo[6] , Federica Ricci[7,8] , Meredith C. Powell[9] , Claudio Ricci[10,11,12] , Richard Mushotzky[13] ,
Franz E. Bauer[2,14,15] , Tonima T. Ananna[16] , Rudolf E. Bär[17] , Bernhard Brandl[1] , Jarle Brinchmann[18,19] ,
Fiona Harrison[20] , Kohei Ichikawa[21,22] , Darshan Kakkad[23] , Kyuseok Oh[24,25] , Rogério Riffel[26,27] , Lia F. Sartori[17] ,
Krista L. Smith[28] , Daniel Stern[29] , and C. Megan Urry[30]

[1] Leiden Observatory, P.O. Box 9513, 2300 RA, Leiden, The Netherlands; caglar@strw.leidenuniv.nl
[2] Eureka Scientific, 2452 Delmer Street, Suite 100, Oakland, CA 94602-3017, USA
[3] Space Science Institute, 4750 Walnut Street, Suite 205, Boulder, CO 80301, USA
[4] School of Physics and Astronomy, Tel Aviv University, Tel Aviv 69978, Israel
[5] Yildiz Technical University, Graduate School of Natural and Applied Sciences, Istanbul 34220, Turkey
[6] European Southern Observatory, Casilla 19001, Santiago 19, Chile
[7] Dipartimento di Matematica e Fisica, Università degli Studi Roma Tre, via della Vasca Navale 84, I-00146, Roma, Italy
[8] INAF—Osservatorio Astronomico di Roma, via Frascati 33, I-00044 Monte Porzio Catone, Italy
[9] Kavli Institute for Particle Astrophysics and Cosmology, Stanford University, 452 Lomita Mall, Stanford, CA 94305, USA
[10] Núcleo de Astronomía de la Facultad de Ingeniería, Universidad Diego Portales, Av. Ejército Libertador 441, Santiago, Chile
[11] Kavli Institute for Astronomy and Astrophysics, Peking University, Beijing 100871, People's Republic of China
[12] George Mason University, Department of Physics & Astronomy, MS 3F3, 4400 University Drive, Fairfax, VA 22030, USA
[13] Department of Astronomy and Joint Space-Science Institute, University of Maryland, College Park, MD 20742, USA
[14] Instituto de Astrofísica and Centro de Astroingeniería, Facultad de Física, Pontificia Universidad Católica de Chile, Casilla 306, Santiago 22, Chile
[15] Millennium Institute of Astrophysics (MAS), Nuncio Monseñor Sótero Sanz 100, Providencia, Santiago, Chile
[16] Department of Physics and Astronomy, Dartmouth College, 6127 Wilder Laboratory, Hanover, NH 03755, USA
[17] Institute for Particle Physics and Astrophysics, ETH Zürich, Wolfgang-Pauli-Strasse 27, CH-8093 Zürich, Switzerland
[18] Centro de Astrofísica da Universidade do Porto, Rua das Estrelas, 4150-762 Porto, Portugal
[19] Instituto de Astrofísica e Ciências do Espaço, Universidade do Porto, CAUP, Rua das Estrelas, 4150-762 Porto, Portugal
[20] Cahill Center for Astronomy and Astrophysics, California Institute of Technology, Pasadena, CA 91125, USA
[21] Astronomical Institute, Tohoku University, Aramaki, Aoba-ku, Sendai, Miyagi 980-8578, Japan
[22] Frontier Research Institute for Interdisciplinary Sciences, Tohoku University, Sendai 980-8578, Japan
[23] Space Telescope Science Institute, 3700 San Martin Drive, Baltimore, MD 21218, USA
[24] Korea Astronomy & Space Science Institute, 776, Daedeokdae-ro, Yuseong-gu, Daejeon 34055, Republic of Korea
[25] Department of Astronomy, Kyoto University, Kitashirakawa-Oiwake-cho, Sakyo-ku, Kyoto 606-8502, Japan
[26] Departamento de Astronomia, Universidade Federal do Rio Grande do Sul, Av. Bento Gonçalves 9500, 91501-970 Porto Alegre, RS, Brazil
[27] Instituto de Astrofísica de Canarias, Calle Vía Láctea s/n, E-38205 La Laguna, Tenerife, Spain
[28] Department of Physics and Astronomy, Texas A&M University, College Station, TX 77843, USA
[29] Jet Propulsion Laboratory, California Institute of Technology, 4800 Oak Grove Drive, MS 169-224, Pasadena, CA 91109, USA
[30] Yale Center for Astronomy & Astrophysics and Department of Physics, Yale University, P.O. Box 208120, New Haven, CT 06520-8120, USA

Abstract

We present two independent measurements of stellar velocity dispersions ($\sigma_\star$) from the Ca II H+K λ3969, 3934 and Mg I b λ 5183, 5172, 5167 region (3880–5550 Å) and the calcium triplet region (8350–8750 Å) for 173 hard X-ray-selected Type 1 active galactic nuclei (AGNs; $z \leqslant 0.08$) from the 105 month Swift-BAT catalog. We construct one of the largest samples of local Type 1 AGNs that have both single-epoch *virial* black hole mass ($M_{\rm BH}$) estimates and $\sigma_\star$ measurements obtained from high spectral resolution data, allowing us to test the usage of such methods for supermassive black hole studies. We find that the two independent $\sigma_\star$ measurements are highly consistent with each other, with an average offset of only 0.002 ± 0.001 dex. Comparing $M_{\rm BH}$ estimates based on broad emission lines and stellar velocity dispersion measurements, we find that the former is systematically lower by ≈ 0.12 dex. Consequently, Eddington ratios estimated through broad-line $M_{\rm BH}$ determinations are similarly biased (but in the opposite way). We argue that the discrepancy is driven by extinction in the broad-line region. We also find an anticorrelation between the offset from the $M_{\rm BH}$–$\sigma_\star$ relation and the Eddington ratio. Our sample of Type 1 AGNs shows a shallower $M_{\rm BH}$–$\sigma_\star$ relation (with a power-law exponent of ≈ 3.5) compared with that of inactive galaxies (with a power-law exponent of ≈ 4.5), confirming earlier results obtained from smaller samples.

1. Introduction

Supermassive black holes (SMBHs), residing in the centers of massive galaxies, are commonly thought to coevolve with their host galaxies, as demonstrated by the present-day correlations between SMBH mass ($M_{\rm BH}$) and several host properties (e.g., Kormendy & Ho 2013; McConnell & Ma 2013;

Saglia et al. 2016), such as the stellar velocity dispersion ($\sigma_\star$) (Ferrarese & Merritt 2000; Gebhardt et al. 2000; Merritt & Ferrarese 2001; Tremaine et al. 2002; Gültekin et al. 2009), bulge luminosity (Kormendy & Richstone 1995; Marconi & Hunt 2003), and bulge mass (Magorrian et al. 1998; Häring & Rix 2004). Additionally, correlations with the bulge's average spherical density, half-mass–radius (e.g., Saglia et al. 2016), and dark matter halos (e.g., Ferrarese 2002; Baes et al. 2003; Bandara et al. 2009; Volonteri et al. 2011; Sabra et al. 2015; Marasco et al. 2021; Powell et al. 2022), have been proposed. Of these, the M_{BH}–$\sigma_\star$ relation is still the tightest relation among them (with an intrinsic scatter of ∼0.3 dex; e.g., Gültekin et al. 2009; Saglia et al. 2016; van den Bosch 2016).

The observed close relations between M_{BH} and host properties strongly support a coevolutionary scenario, where some form of *feedback* exerted by actively accreting SMBHs (i.e., active galactic nuclei (AGNs)) affects the host galaxy growth. Indeed, specific feedback models have been shown to be related to the shape of the M_{BH}–$\sigma_\star$ relation, and in particular, its exponent, β (where $M_{\mathrm{BH}} \propto \sigma_\star^\beta$), with $\beta \simeq 4$ attributed to momentum-driven feedback and $\beta \simeq 5$ attributed to energy-driven feedback (Silk & Rees 1998; King 2003, respectively). Observationally, the details and impact of AGN feedback, as well as the slope β are not yet settled. Kormendy & Ho (2013, hereafter KH13) find $\beta = 4.38$ using spatially resolved gas and stellar kinematics for elliptical and classical bulge hosting local galaxies. However, (McConnell & Ma 2013, hereafter MM13) report an $\beta = 5.64$ using M_{BH} estimates from spatially resolved dynamics in a sample of local early- and late-type galaxies (including brightest cluster galaxies). Both these samples and indeed most samples used for such studies, are dominated by inactive galaxies with the presence of just a few low-luminosity AGNs. Finally, van den Bosch (2016) reports a $\beta = 5.35$ using a sample of galaxies in which SMBH masses are compiled using four different methods: gas dynamics, stellar dynamics, reverberation mapping, and mega-masers.

Recent studies have suggested whether SMBH-host relations may depend on a variety of factors, including host morphology. Specifically, early- versus late-type galaxies (e.g., Gültekin et al. 2009; McConnell & Ma 2013), pseudo- versus real bulges (e.g., Greene et al. 2010; Kormendy & Ho 2013; Ho & Kim 2014), and barred versus unbarred galaxies (e.g., Graham 2008; Hu 2008; Graham & Li 2009; Hartmann et al. 2014) have all been discussed as possible influencing factors. Additionally, Xiao et al. (2011) found a small offset caused by the disk inclination. Interestingly, some studies have shown a $\beta \approx 3$ for galaxies with pseudo-bulges (e.g., Greene et al. 2010; Ho & Kim 2014). However, pseudo-bulge hosting galaxies are found to have an order of magnitude lower black hole masses relative to elliptical bulge hosting galaxies (e.g., Greene et al. 2010; Ho & Kim 2014), and thus, reside significantly below the M_{BH}–$\sigma_\star$ relation of inactive galaxies, and they also show a larger scatter at the lower-mass end.

For actively accreting SMBHs (i.e., AGNs) the primary approach for M_{BH} determination is the reverberation mapping (RM) of broad emission lines (e.g., Blandford & McKee 1982; Peterson 1993; Onken & Peterson 2002; Bentz et al. 2006b; Denney et al. 2006; Bentz et al. 2009a, 2009b; Denney et al. 2010; Bentz et al. 2016; Villafaña et al. 2022). Despite several dedicated campaigns in recent years, the number of reliable M_{BH} determinations remains limited to ≈90 systems (see the

RM black hole mass archive; Bentz & Katz 2015). Several recent and ongoing RM campaigns aim to significantly increase the number of RM-based M_{BH} measurements, such as OzDES-RM (Yuan et al. 2015), the Sloan Digital Sky Survey (SDSS)-RM (Shen et al. 2015, 2016), and SDSS-V (Kollmeier et al. 2017).

The so-called single-epoch (SE) M_{BH} estimation method provides a potential solution to estimate M_{BH} for the much larger spectroscopic data sets of Type 1 AGNs, including luminous quasars that can be traced to $z \gtrsim 7$. The method uses the width of the broad emission lines (either FWHM or standard deviation σ) as a proxy for the virialized broad-line-region (BLR) gas velocities and the AGN continuum luminosity as a probe of the BLR radius. The latter is based on relatively tight correlations between BLR size and AGN continuum luminosity in various spectral bands (e.g., Koratkar & Gaskell 1991; Kaspi et al. 2000, 2005; Bentz et al. 2006a, 2009b; Zajaček et al. 2020). Since the BLR geometry and (detailed) radiative physics are not entirely known (per source), the SE method adopts an order-of-unity scaling factor to yield M_{BH}. Crucially, this scaling factor called the *virial factor* (f) is typically derived by *assuming* that AGNs follow the same M_{BH}–$\sigma_\star$ relation as the one determined for inactive galaxies. Indeed, the systematic uncertainty of M_{BH} estimates derived using the SE method can reach $\gtrsim$0.4 dex (Pancoast et al. 2014; Ricci et al. 2017c; Caglar et al. 2020), mostly due to the intrinsic scatter in the M_{BH}–$\sigma_\star$ relation.

An average virial factor of $f_{\mathrm{FWHM}} \approx 1$ is reported with an uncertainty of 0.15 dex by calibrating RM-based M_{BH} estimations to various versions of the M_{BH}–$\sigma_\star$ relation (e.g., Onken et al. 2004; Park et al. 2012; Grier et al. 2013; Woo et al. 2013, 2015; Grier et al. 2017). Several studies have investigated in detail the M_{BH}–$\sigma_\star$ relation for AGNs by combining RM-based virial M_{BH} determinations and host $\sigma_\star$ measurements (e.g., Nelson et al. 2004; Onken et al. 2004; Woo et al. 2010; Graham et al. 2011; Park et al. 2012; Woo et al. 2013, 2015; Batiste et al. 2017; Bennert et al. 2021). Generally, the slope of the M_{BH}–$\sigma_\star$ relation for RM AGNs is found to be shallower than that of inactive galaxies ($\beta \lesssim 4$; e.g., Woo et al. 2013, 2015; Bennert et al. 2021), but the discrepancy between the two relations is often attributed to unreliable $\sigma_\star$ measurements in AGN-dominated spectra of Type 1 AGNs, as well as due to sample selection bias (e.g., Greene & Ho 2006; Lauer et al. 2007; Shen 2013; Shankar et al. 2016). Interestingly, Caglar et al. (2020, hereafter C20) have proposed that some part of the discrepancy might be caused by extinction in the BLR, which was also claimed by Mejía-Restrepo et al. (2022) and Ricci et al. (2022). Hence, the discrepancies between the M_{BH}–$\sigma_\star$ relations of active and inactive galaxies may reflect real, though yet unclear, astrophysical differences between these populations. Clearly, detailed analyses of large and highly complete AGN samples and inactive galaxies are needed to address the origin of such discrepancies.

In this work, we present stellar velocity dispersion measurements for a sample of broad-line, Type 1 AGNs drawn from the second data release of the Swift/BAT AGN Spectroscopic Survey (BASS DR2[31]; Koss et al. 2022a). BASS is a highly complete survey of ultra-hard X-ray-selected AGNs, mainly in the local universe. The ultra-hard X-ray selection (14–195 keV) allows

---

[31] www.bass-survey.com

us to overcome biases related to (circumnuclear) obscuration (e.g., Ricci et al. 2015, 2017a), host properties, etc., thus, potentially circumventing some of the challenges faced by previous studies. We aim to study the $M_{\rm BH}$–$\sigma_\star$ relation for our sample and compare our results with the $M_{\rm BH}$–$\sigma_\star$ relation for inactive galaxies. We additionally investigate a potential discrepancy between two black hole mass estimates obtained from the SE method versus the ones from the $M_{\rm BH}$–$\sigma_\star$ relation. Throughout this paper, we define this discrepancy as the offset from the $M_{\rm BH}$–$\sigma_\star$ relation as follows: $\Delta\mathcal{M}_{\rm BH} \equiv \log M_{\rm BH,BLR} - \log M_{\rm BH,\sigma}$. Finally, we aim to understand how such discrepancies may depend on several key AGN properties. This paper is organized as follows. In Section 2, we introduce the BASS-based AGN sample and archival data. In Section 3, we describe our analysis methodology, while in Section 4 we present and discuss our main results. We conclude with a summary of our key findings in Section 5. Throughout this paper, we assume a standard flat Lambda cold dark matter cosmology, with $H_0 = 70\ {\rm km\ s^{-1}\ Mpc^{-1}}$, $\Omega_{\rm M} = 0.3$, and $\Omega_\Lambda = 0.7$.

2. BASS Sample and Archival Data

The 70 month data release of Swift-BAT hard X-ray (14–195 keV) all-sky survey (Baumgartner et al. 2013) consists of 858 AGNs. BASS aims to obtain optical spectroscopy for BAT-selected AGNs. Specifically, BASS DR2 includes optical spectra for essentially all 70 month BAT catalog AGNs, except for six highly extincted sources located at Galactic latitudes $|b| < 10°$. We also use BASS-led spectroscopy of AGNs drawn from the 105 month BAT survey (Oh et al. 2018). Although this effort is not yet complete and does not represent a flux-limited sample, the spectra in hand allow us to probe fainter sources, extending the range in SMBH mass and/or Eddington ratio under study.

The targeted optical spectroscopy pursued by BASS typically covers a wide spectral range (3000–10,000 Å), in order to study both AGN-dominated broad and narrow emission lines (e.g., Mejía-Restrepo et al. 2022; Oh et al. 2022; Ricci et al. 2022) and host galaxy properties (e.g., Koss et al. 2022b; Powell et al. 2022). Key technical aspects of the spectra used for our work are provided in Section 3.1, where we detail our spectral measurements. We stress that the ultra-hard X-ray Swift-BAT survey allows us to detect AGNs with a wide range of neutral hydrogen absorbing columns, ranging from unabsorbed ($\log(N_{\rm H}/{\rm cm}^{-2}) = 20.0$) to Compton-thick ($\log(N_{\rm H}/{\rm cm}^{-2}) > 24.0$) sources. Indeed, the BASS sample was shown to be less biased compared to other surveys with respect to obscuration (e.g., Ricci et al. 2015; Koss et al. 2016; Ricci et al. 2022), star formation (e.g., Shimizu et al. 2015; Ichikawa et al. 2017, 2019), and host molecular gas content (Koss et al. 2021). More detailed information about BASS DR2 can be found in the main BASS DR2 overview and catalog papers (Koss et al. 2022a, 2022c).

2.1. Our Sample

The BASS DR2 sample comprises 858 AGNs: 359 of which are classified as Type 1 sources, 393 Type 2 (including Seyfert 1.9 sources), and 106 beamed and/or lensed AGNs (see Koss et al. 2022a, 2022c, for more details). Importantly for this work, we note that the velocity dispersion measurements for the obscured AGNs in BASS DR2 (Seyfert 1.9 and 2 AGNs) are presented in Koss et al. (2022b). Here we focus only on

Type 1 AGNs with redshifts $z \leqslant 0.08$, where the redshift threshold is chosen in order to avoid telluric absorption across the calcium triplet (CaT) absorption complex. Furthermore, we excluded 40 Type 1 AGN spectra observed with low-resolution spectral setups ($R < 1000$), where $\sigma_\star$ measurements would be unreliable. Our final sample thus consists of a total of 240 AGNs, of which 185 are from the 70 month BAT catalog and 55 are a *bonus* sample from the 105 month catalog.

2.2. BASS Archival Data

2.2.1. X-Ray Data

We adopted hydrogen column density measurements ($N_{\rm H}$) and intrinsic (absorption-corrected) X-ray luminosity measurements, and related uncertainties (90% confidence intervals) directly from Ricci et al. (2017b) for the 70 month Swift-BAT sources in our sample. These are obtained by fitting the X-ray spectra with a variety of models, including an absorbed cutoff power-law component, an unobscured reflection component, and another cutoff power-law component for scattering. We note that there are no $N_{\rm H}$ or intrinsic X-ray luminosity determinations available for the bonus sample of AGNs from the 105 month Swift-BAT catalog.

2.2.2. Black Hole Masses

We adopt broad-line-based SE (*virial*) black hole mass estimates for our sample of AGNs from the respective BASS DR2 catalog of Mejía-Restrepo et al. (2022). That study performed a detailed spectral decomposition and emission line fitting procedure, following Trakhtenbrot & Netzer (2012) and Mejía-Restrepo et al. (2016). In Mejía-Restrepo et al. (2022), $M_{\rm BH}$ is calculated using the prescriptions calibrated by Greene & Ho (2005) for Hα and Trakhtenbrot & Netzer (2012) for Hβ, and using the FWHM of the emission lines and a virial factor of $f = 1$. The latter choice results in a somewhat revised $M_{\rm BH}$ prescription (i.e., compared with the one presented in Greene & Ho 2005), of the form

$$M_{\rm BH} = 2.67 \times 10^6 \times \left(\frac{L_{\rm H\alpha}}{10^{42}\ {\rm erg\ s^{-1}}}\right)^{0.55} \left(\frac{\rm FWHM_{\rm H\alpha}}{10^3\ {\rm km\ s^{-1}}}\right)^{2.06} M_\odot,$$

(1)

where the Hα related quantities reflect only the broad emission component. A detailed explanation of the fitting procedure and this $M_{\rm BH}$ prescription, as well as a complete catalog of the best-fitting parameters, can be found in Mejía-Restrepo et al. (2022). Here, we note that Mejía-Restrepo et al. (2022) only corrected their $M_{\rm BH}$ estimates for the Galactic extinction, but in this work, we will even further correct their $M_{\rm BH}$ estimates for the BLR extinction, which will be described in Section 3.2.

3. Analysis and Methods

3.1. Stellar Velocity Dispersion Measurements

We measure host galaxy stellar velocity dispersion for our sample of Type 1 AGNs using the penalized pixel-fitting procedure (pPXF; Cappellari & Emsellem 2004; Cappellari 2017). The pPXF routine applies the Gauss–Hermite parameterization for the line-of-sight velocity distribution in pixel space. By using pPXF, the continuum can be matched using additive polynomials, whereas bad pixels and/or emission lines

Table 1
Stellar Velocity Dispersions and Key Derived Properties of Our AGNs

BAT ID	Galaxy Name	σ_{blue} (km s^{-1})	flag$_B$	σ_{red} (km s^{-1})	flag$_R$	A_V (mag)	$\log \lambda_{\mathrm{Edd}}$	$\log \lambda_{\mathrm{Edd,corr}}$	$\dot{M}$ ($M_\odot$ yr^{-1})	Instrument
1	2	3	4	5	6	7	8	9	10	11
3	NGC7811	88 ± 14	0	91 ± 8	0	0.131	−0.924	−0.943	0.022	Palomar/DBSP
34	UGC524	156 ± 5	0	157 ± 4	0	1.586	−0.853	−1.146	0.043	Palomar/DBSP
43	Mrk352	97 ± 6	0	95 ± 8	0	0.207	−1.582	−1.621	0.021	Palomar/DBSP
45	LEDA 1075692	195 ± 7	0	196 ± 6	0	2.668	−1.081	−1.564	0.139	VLT/X-Shooter
51	RBS149	…	9	134 ± 28	2	0	−0.939	−0.939	0.168	Palomar/DBSP
52	HE0103-3447	…	9	182 ± 21	2	0	−1.404	−1.404	0.155	VLT/X-Shooter
60	Mrk 975	…	9	149 ± 9	1	0.146	−1.127	−1.152	0.112	Keck/LRIS
61	Mrk1152	168 ± 7	0	170 ± 5	0	1.78	−1.07	−1.39	0.221	Palomar/DBSP
73	Fairall9	…	9	219 ± 14	1	0	−1.138	−1.138	0.336	VLT/X-Shooter
77	Mrk359	90 ± 15	2	101 ± 10	2	0	−0.372	−0.372	0.012	VLT/X-Shooter

Notes. We list the columns in this table as follows. (1) Catalog ID from the 105 month SWIFT-BAT survey. (2) Host galaxy. (3) Stellar velocity dispersion measurement from the Ca II H+K λ3969, 3934 & Mg I b λ 5183, 5172, 5167 region (3880–5550 Å). (4) The quality flag for σ_{blue} fit. (5) Stellar velocity dispersion measurement from the Calcium Triplet region (CaT, 8350–8750 Å). (6) Quality flag for σ_{red} fit. (7) Dust extinction in the BLR. (8) The extinction-uncorrected Eddington ratio. (9) The extinction-corrected Eddington ratio. (10) Accretion rate. (11) The instrument used for the observation. (A portion of the table is shown here for visual guidance and the entire table can be found in machine-readable form.)

(This table is available in its entirety in machine-readable form.)

can be masked from the spectra. Finally, pPXF makes initial guesses for $\sigma_\star$ by broadening the stellar templates. During this procedure, several parameters are being fit simultaneously, including the systemic velocity (V), the velocity dispersion (σ), and a series of Hermite polynomials, $h_3 ... h_m$.

In our study, we performed the pPXF method allowing the following parameters as free: the systemic velocity (V), the velocity dispersion (σ), and two Hermite polynomials (h_3 and h_4). We supplemented pPXF with a grid of stellar spectral templates based on VLT/X-shooter observations (Chen et al. 2014; Gonneau et al. 2020) using the velocity scale ratio of 2, which corresponds to the templates at twice the resolution of the observed spectra. The X-shooter Spectral Library we used contains 830 stellar spectra of 683 stars covering the wavelength range of 3500–24,800 Å with an average instrumental resolution of 0.51 Å for the bluer spectral regions of interest (3800–5500 Å) and 0.78 Å for the red spectral region (8300–8800 Å). However, our sample of galaxies is observed by various instruments with a variety of spectral resolutions ranging from 2.0–6.0 Å (3800–5500 Å).[32]

Therefore, the template spectra were convolved with a relative line-spread function. We masked several prominent, mostly AGN-dominated emission lines that are present in our spectral regions of interest (H$\beta, \gamma, \delta, \epsilon$, [Ne III] λ 3968, [O III $\lambda\lambda$ 4959,5007], O I λ8446, and Fe II λ8616), as well as bad pixels (if these exist), to increase the robustness of our $\sigma_\star$

measurements. To mask broad emission components, we additionally applied a mask function with a range of width 2000–3500 km s^{-1}, which is appropriate for the BLR-related widths of our broad-line AGNs. We performed pPXF fitting adopting additive (between degree = 2–8) and multiplicative (mdegree = 0–1) polynomials to develop the best match between the composite stellar population and the galaxy spectrum. We finally selected the best-fit result with the least possible degree of polynomials. To estimate the uncertainties associated with $\sigma_\star$ measurements, we used the suggested residuals bootstrapping procedure (Cappellari 2022). Briefly, for each AGN, we resample the residuals of the initial $\sigma_\star$ fit to generate 100 mock spectra to perform 100 additional fits, resulting in a distribution of $\sigma_\star$ measurements as well as uncertainties in the distribution of the weights. The same bootstrapping approach was also used by Koss et al. (2022b) for DR2 type 2 (Seyfert 1.9 and 2) AGNs.

In Table 1, we present the resulting $\sigma_\star$ measurements from the spectral region covering Ca H+K and Mg I, and/or the CaT features (henceforth σ_{blue} and σ_{red}, respectively) for our sample of AGNs. Additionally, the pPXF model fits are shown in Appendix A (Figure 7(a), (b)). Three experienced coauthors (T. C., L.B., and M.K.) have visually inspected the spectral fits and assigned a quality flag for each spectral region of each AGN: 0 for good quality fits, 1 for acceptable fits, 2 for unaccepted fits, and 9 for failed fits (see Table 2). For most sources, we were able to fit both the blue part and the red part of the spectra to obtain independent $\sigma_\star$ measurements. For the SOAR spectra, we only fit the CaT features region since the instrumental setup only covers that spectral region. Here, we note that, for some of

---

[32] We also have spectral data from low-resolution observation setups ($R < 1000$), which are not taken into consideration for $\sigma_\star$ measurements (see Koss et al. 2022c).

Table 2
Stellar Velocity Dispersions Failures

BAT ID	Galaxy Name	Reason	z	$E(B–V)$ (mag)	L_{bol} (erg s^{-1})	Seyfert Type	Instrument
1	2	3	4	5	6	7	8
6	Mrk335	AGN	0.0259	0.0354	44.29	Sy 1.2	Palomar/DBSP
22	Z535-12	AGN	0.0476	0.0666	44.84	Sy 1.2	Palomar/DBSP
36	Mrk1148	AGN	0.064	0.057	45.35	Sy 1.5	Palomar/DBSP
78	MCG-3-4-72	AGN	0.0429	0.0188	44.84	Sy 1	Palomar/DBSP
113	LEDA138501	AGN	0.0497	0.1628	45.42	Sy 1	Palomar/DBSP
122	2MASXJ02223523+2508143	Resolution	0.0616	0.08	45.05	Sy 1	Palomar/DBSP
130	Mrk1044	AGN	0.0173	0.0334	43.81	Sy 1	VLT/X-Shooter
143	Rhs15	Low S/N	0.0697	0.0662	44.98	Sy 1	Palomar/DBSP
147	Q0241+622	AGN	0.0447	0.7427	45.54	Sy 1.2	Palomar/DBSP
161	2MASXJ02593756+4417180	Resolution	0.0313	0.2206	44.39	Sy 1	Palomar/DBSP

Notes. Column descriptions: (1) Catalog ID from the SWIFT-BAT survey, (2) host galaxy, (3) reason for failure. AGN: spectra were dominated by AGN emission lines contaminating the absorption lines, low signal-to-noise ratio (S/N). Resolution: no suitable high-resolution spectra were available, and GalExt: high Galactic extinction. (4) Redshift. (5) Interstellar reddening. (6) The bolometric AGN luminosity. (7) AGN type based on optical spectroscopy. (8) Best available spectra from DR2. See Koss et al. (2022c) and Mejía-Restrepo et al. (2022) for more details on redshift and Seyfert types. (A portion of the table is shown here for visual guidance and the entire table can be found in machine-readable form.)

(This table is available in its entirety in machine-readable form.)

our AGNs, we have multiple spectra obtained with different instruments. In Appendix B, we show a comparison of $\sigma_\star$ measurements from the different instruments.

3.2. Extinction in the BLR

In virial, SE M_{BH} estimators, either monochromatic or line luminosity (e.g., λL_λ [5100 Å] or $L_{H\alpha}$) are used as a probe of the BLR radius. These prescriptions are fundamentally based on RM studies, in which the targets are assumed to be unobscured Type 1 AGNs. However, in the presence of dust extinction along the line of sight, a correction should be applied to the observed line luminosities. In previous work, C20 demonstrated that applying extinction correction reduces $\Delta \mathcal{M}_{BH}$ by $\sim$0.3–0.4 dex for their sample of 10 Type 1 and 3 Type 2 AGNs. Here, we remind readers that $\Delta \mathcal{M}_{BH}$ corresponds to the difference in M_{BH} between the SE measurements and the $\sigma_\star$ based measurements.

In Section 4.4.1, we discuss the importance of extinction correction for the BLR-based estimates of M_{BH}. We use intrinsic ultra-hard X-ray luminosities to obtain extinction-corrected Hα luminosities in the BLR, assuming that the BLR extinction of Hα emission is purely due to attenuation by dust (Shimizu et al. 2018):

$$\log L_{H\alpha}^{corr} = 1.117 \times \log(L_{14-150\,keV}^{int}) - 6.61 \quad erg\ s^{-1}, \quad (2)$$

where $L_{14-150\,keV}^{int}$ is the intrinsic X-ray luminosity integrated over the 14–150 keV energy range and $L_{H\alpha}^{corr}$ is the intrinsic (i.e., extinction-corrected) broad Hα luminosity. Here, we note that we adopt the updated $\log L_{14-150\,keV} - \log L_{H\alpha}$ correlation parameters (T. Shimizu, private communication) and that this correction introduces an additional systematic uncertainty of $\sim$0.2 dex to the associated M_{BH} estimates (i.e., through Equation (1)).

However, since we do not have intrinsic ultra-hard X-ray luminosities in the 14–150 keV energy band ($\log(L_{14-150\,keV}^{int}/erg\ s^{-1})$) for our bonus sample of 55 AGNs, we will use the observed ultra-hard X-ray luminosities in the 14–195 keV energy band

($\log(L_{14-195\,keV}^{obs}/erg\ s^{-1})$) as alternatives for $\log(L_{14-150\,keV}^{int}/erg\ s^{-1})$ estimates (see Appendix C).

Next, we used the observed and corrected Hα luminosities to estimate the level of optical extinction ($A_{H\alpha}$) for each source. This is done by deriving the extinction, in magnitudes, affecting Hα,

$$A_{H\alpha} = 2.5 \times (\log L_{H\alpha}^{corr} - \log L_{H\alpha}^{obs}) \quad mag, \quad (3)$$

and then deriving the extinction at any wavelength λ following the empirically determined extinction law of Wild et al. (2011):

$$\frac{A_\lambda}{A_V} = 0.6\left(\frac{\lambda}{5500\ Å}\right)^{-1.3} + 0.4\left(\frac{\lambda}{5500\ Å}\right)^{-0.7}. \quad (4)$$

This extinction law is particularly appropriate for AGNs with a large dust reservoir (e.g., Wild et al. 2011; Schnorr-Müller et al. 2016). Here, we note that deriving the extinction in the BLR cannot be done by simple Balmer decrement method (i.e., Hα/Hβ), as the photoionization models predict a wide range of theoretical BLR line ratios for AGNs depending on their BLR conditions (Schnorr-Müller et al. 2016). Finally, we correct the M_{BH} estimates reported by Mejía-Restrepo et al. (2022) for the BLR extinction (see Appendix D for a discussion of the difference between extinction-corrected/uncorrected estimates).

3.3. Eddington Ratio and Accretion Rates

In order to estimate the Eddington ratios ($\log \lambda_{Edd}$), we follow the same approach used in BASS DR1 (Koss et al. 2017). First, we convert the intrinsic, absorption-corrected hard X-ray luminosities ($L_{2-10\,keV}^{int}$) to bolometric luminosities (L_{bol}) using a universal bolometric correction, that is $L_{bol} = 20 \times L_{2-10\,keV}^{int}$. Although this simple bolometric correction may carry significant uncertainties (i.e., $\approx 20^{+60}_{-10}$) and likely depends on various AGN properties (see, e.g., Marconi et al. 2004; Vasudevan et al. 2009), we note that it was shown to be fairly constant for low-luminosity AGNs ($\log(L_{2-10\,keV}/erg\ s^{-1}) \lesssim 45$; see, e.g., the
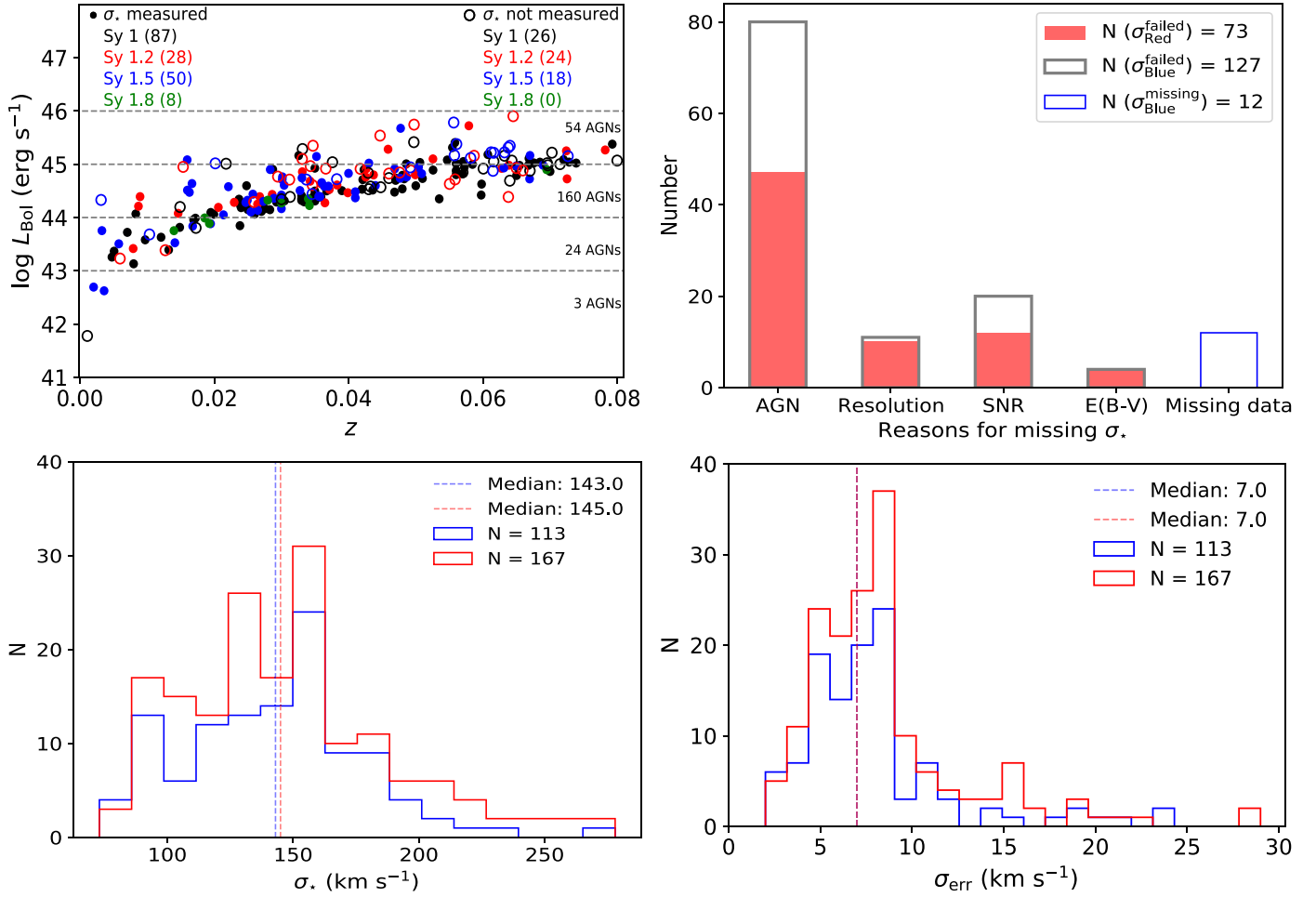
Figure 1. Top left: the bolometric AGN luminosities vs. redshift for our sample of AGNs. We show AGNs with successful $\sigma_\star$ fits with filled circles, while those with failed $\sigma_\star$ fits are shown with open circles. Top right: distributions of failed $\sigma_{\rm blue}$ (based on the region covering the Ca H+K and Mg I absorption lines) and $\sigma_{\rm red}$ (based on the region that covers the CaT absorption lines) measurements are separated by failure reason. Bottom left: distributions of successful velocity dispersion fit results. Bottom right: distributions of measurement errors for successful velocity dispersion measurements. Blue histograms represent $\sigma_{\rm blue}$, whereas red histograms represent $\sigma_{\rm red}$. The vertical blue and red lines correspond to the median values for $\sigma_{\rm blue}$ and $\sigma_{\rm red}$, respectively.

study of Duras et al. (2020), which relies on the Swift-BAT AGN sample). Therefore, the fact that the majority of our sample is dominated by such low-luminosity AGNs further justifies the use of a universal bolometric correction.

The Eddington luminosities ($L_{\rm Edd}$) of our sources are calculated as $L_{\rm Edd} = 1.26 \times 10^{38}\, M_{\rm BH}/M_\odot$, which is appropriate for pure hydrogen gas. Finally, the Eddington ratios are calculated following $\log \lambda_{\rm Edd} \equiv L_{\rm bol}/L_{\rm Edd}$. We emphasize that the large uncertainty in $L_{\rm Bol}$ ($\sim$0.3–0.6 dex) and $M_{\rm BH}$ ($\sim$0.4 dex) contributes to the (systematic) uncertainty of the Eddington ratio, which is likely $\gtrsim$0.7 dex in total (e.g., Bian & Zhao 2003; Marinucci et al. 2012). We also estimate the physical accretion rates ($\dot{M}$) that power the AGNs in our sample, through $\dot{M} = L_{\rm bol}/(\eta c^2)$, assuming a standard radiative efficiency of $\eta = 0.1$.

4. Results and Discussion

In this work, we measured $\sigma_\star$ of broad-line Type 1 AGNs from the BASS DR2 sample. In the top-left panel of Figure 1, we present an overview of our sample of AGNs for successful (173) and failed (68) $\sigma_\star$ fit results. The majority of $\sigma_\star$ measurements are obtained from the CaT spectral region (167 successful and 74 failed fits), but whenever available, we provide the resulting $\sigma_\star$

measurements from the Ca H+K and Mg I absorption lines (113 successful and 116 failed fits). There are also 12 missing fits (see the top-right panel of Figure 1). For eight of these (BAT IDs: 184, 301, 558, 607, 631, 680, 1046, 1142) we adopt $\sigma_\star$ measurements from the LLAMA study by C20. The remaining five cases lack the appropriate spectral coverage due to the BASS observational setup available at the time of writing.

In what follows, we discuss the issues related to sample (in) completeness; present a comparison between the $\sigma_{\rm blue}$ and $\sigma_{\rm red}$ measurements, explore the systematic uncertainties caused by aperture size, and show a direct comparison between our $\sigma_\star$ measurements and those available from other surveys. We then use BASS archival data to address the possible reasons for the offset from the $M_{\rm BH}$–$\sigma_\star$ relation by looking into trends with key parameters such as BLR extinction, redshift, intrinsic X-ray luminosity, and Eddington ratio. Finally, we present the resulting $M_{\rm BH}$–$\sigma_\star$ relation for our sample of Type 1 AGNs.

4.1. Stellar Velocity Dispersion Measurements

4.1.1. Sample (In)completeness

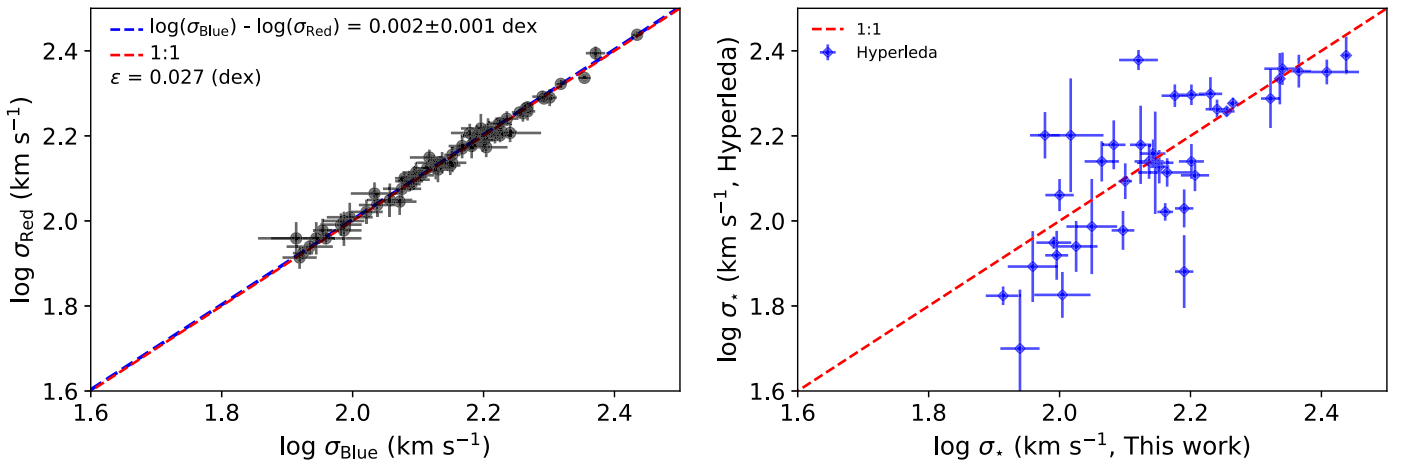Thanks to the high-resolution observations with instruments such as VLT/X-shooter, SOAR/Goodman, and Palomar/DBSP,

Figure 2. Left: comparison between $\sigma_{\rm blue}$ and $\sigma_{\rm red}$ measurements. The blue dashed line represents the difference in both measurements. The red dashed lines represent 1:1 lines in both panels. Right: comparison between our best-fitting $\sigma_\star$ results vs. the $\sigma_\star$ results in the literature.

our sample is free of biases caused by insufficient spectral resolution. The spectral setups used for this work provide an instrumental resolution of $\sigma_{\rm inst} = 19$–$27\,{\rm km\,s^{-1}}$, which allows us to measure $\sigma_\star$ of intermediate SMBH hosting AGNs ($M_{\rm BH} < 10^6$ $M_\odot$). A limited number of our AGNs have been observed with lower spectral resolution setups, as mentioned in Section 3.1, but we emphasize that the low-resolution were not used in $\sigma_\star$ measurements in order to avoid possible biases caused by resolution insufficiency.

We remind the reader that we fit a total number of 240 Type 1 AGN spectra for two distinct spectral regions (3880–5500 Å and 8350–8730 Å, whenever possible). These fits yield independent $\sigma_\star$ measurements based on the Ca H+K and Mg I features, and on the CaT features, respectively. We refer to these independent $\sigma_\star$ measurements as $\sigma_{\rm blue}$ and $\sigma_{\rm red}$ (again, respectively).

Table 1 lists the resulting $\sigma_\star$ measurements from both spectral regions together with the corresponding quality flags. We obtained at least one $\sigma_\star$ measurement for 173 AGNs with small uncertainties. We had 67 failed attempts (see Table 2). For the 173 successful fits, we flag 128 $\sigma_\star$ measurements as good, 35 as acceptable, and 10 as unaccepted fits (quality flags 0, 1, and 2, respectively). We additionally fit 48 duplicate spectra observed with other instruments, yielding 28 successful and 20 failed fits. The top-right panel of Figure 1 presents the main reasons for failed $\sigma_\star$ measurements, including strong AGN emission features (~64% of the failed fits); insufficient signal-to-noise ratio (~16%); insufficient spectral resolution (~14%); and high Galactic extinction (~6%). In addition to these, we also compare our successful and failed $\sigma_\star$ measurements with various AGN properties in Appendix E. See Appendix E for further discussion.

In the bottom panel of Figure 1, we present the distributions of $\sigma_\star$ measurements and their corresponding errors. Looking at the two types of $\sigma_\star$ measurements, our $\sigma_{\rm red}$ measurements are in the range of $73 \leqslant \sigma_{\rm red} \leqslant 278\,{\rm km\,s^{-1}}$, with a median of $145 \pm 7\,{\rm km\,s^{-1}}$, while the $\sigma_{\rm blue}$ measurements are in the range of $82 \leqslant \sigma_{\rm blue} \leqslant 272\,{\rm km\,s^{-1}}$ with a median of $143 \pm 7\,{\rm km\,s^{-1}}$. We compare $\sigma_{\rm red}$ and $\sigma_{\rm blue}$, for the AGNs for which both types of measurements are available, in the left panel of Figure 2. Clearly, the two types of measurements are in excellent agreement, as is supported by a Spearman correlation test

($\rho = 0.98 \pm 0.01$, $p \ll 0.01$).[33] The average offset between the two types of $\sigma_\star$ measurements is small $\langle \log(\sigma_{\rm red}) - \log(\sigma_{\rm blue}) \rangle = 0.002 \pm 0.001$ dex, and the scatter around the 1:1 relation is 0.027 dex. This small level of scatter is probably explained by the somewhat different stellar populations that dominate the absorption features in these spectral regions (see, e.g., Riffel et al. 2015).

4.1.2. Comparison with Other Measurements

We compare our best $\sigma_\star$ measurements with literature measurements from the HyperLeda $\sigma_\star$ catalog (Paturel et al. 2003), which contains a total of nearly of 40,000 $\sigma_\star$ measurements for more than 29,000 objects. We find a total of 39 $\sigma_\star$ measurements, drawn from nine studies (Terlevich et al. 1990; Nelson & Whittle 1995; Oliva et al. 1995, 1999; Wegner et al. 2003; Garcia-Rissmann et al. 2005; Greene & Ho 2006; Ho et al. 2009; Cappellari et al. 2013). In the right panel of Figure 2, we present a comparison between our best $\sigma_\star$ measurements and the corresponding measurements from HyperLeda. The difference in median between our $\sigma_\star$ measurements and those of HyperLeda is ~0.006 dex, which could be caused by aperture differences. Interestingly, our $\sigma_\star$ measurement uncertainties (a median value of 7 ${\rm km\,s^{-1}}$) are typically lower than those reported in HyperLeda (a median value of 13 ${\rm km\,s^{-1}}$). Here, we note that we define the best $\sigma_\star$ measurements using two conditions: (1) the ones with better fit quality among $\sigma_{\rm blue}$ and $\sigma_{\rm red}$ fits and (2) the ones with the smallest uncertainty in $\sigma_\star$.

4.2. M_{BH}–$\sigma_\star$ Relation of BAT Type 1 AGNs

Our sample and measurements enable one of the largest investigations of the M_{BH}–$\sigma_\star$ relation for Type 1 AGNs. We fit our $\log \sigma_\star$ and $\log M_{\rm BH}$ measurements with a linear relation using the bivariate correlated errors and the intrinsic scatter method, which takes into account the measurement errors in both variables (i.e., X and Y axes; Akritas & Bershady 1996;

---

[33] Throughout this paper, p-values (p) are given in three different thresholds (0.01, 0.05, and 0.1). However, we note that these threshold values are represented as upper and lower limits; therefore, the values can be much larger or smaller than reported threshold values. We also note that the Monte Carlo-based bootstrapping method is used to estimate the uncertainty in the Spearman rank correlation coefficient (Curran 2014).
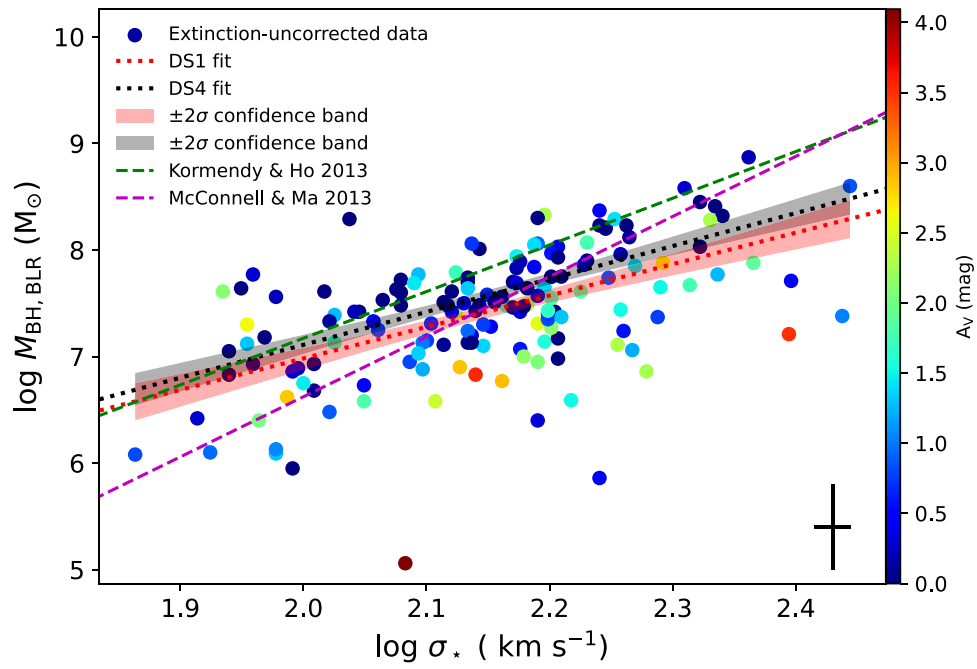
Figure 3. The $M_{BH}-\sigma_\star$ relation of 154 Type 1 AGNs for both extinction-uncorrected and -corrected data sets. The red and black dotted lines represent the resulting $M_{BH}-\sigma_\star$ fits for the DS1 and DS4 subsamples, respectively. We show the median uncertainty in $\sigma_\star$ and M_{BH} as a black plus sign for visual aid.

Table 3
$M_{BH}-\sigma_\star$ Relation Results for Our Data Sets

Subsample[a]	Number	α	β	ϵ
All (no corr)	154	7.87 ± 0.07	2.95 ± 0.41	0.24 ± 0.05
$A_V = 0$	45	8.12 ± 0.10	3.21 ± 0.66	0.38 ± 0.06
$A_V < 1$	99	8.05 ± 0.09	3.44 ± 0.48	0.25 ± 0.04
A_V (corrected)	154	8.04 ± 0.07	3.09 ± 0.39	0.33 ± 0.06

Note.
[a] As suggested by C20, NGC 7213 is removed from the data sets due to its unreliable M_{BH} measurement since this galaxy hosts a low-ionization nuclear emission line region.

Nemmen et al. 2012). The linear regression was performed using the Y/X method, where the slope and intercept can vary. To fit the $M_{BH}-\sigma_\star$ relation, we use a single power-law function as expressed in the following equation:

$$\log(M_{BH}/M_\odot) = \alpha + \beta \log\left(\frac{\sigma_\star}{\sigma_0}\right), \quad (5)$$

where α is the intercept, β is the slope and σ_0 is the normalization coefficient of $200 \ \mathrm{km\,s^{-1}}$. We then performed the linear regression fits for four different data sets, as follows: (1) all our AGNs, without extinction corrections (154 sources; DS1 hereafter); (2) AGNs with negligible extinction, $A_V = 0$ mag (45 sources; DS2 hereafter); (3) AGNs with limited extinction, $A_V < 1$ mag (99 sources; DS3 hereafter); and (4) all AGNs with extinction corrections (154 sources; DS4 hereafter). In Figure 11, we present the resulting $M_{BH}-\sigma_\star$ relations for each of our data sets, while Table 3 lists the best-fit intercepts (α), slopes (β), and intrinsic scatters (ϵ) derived for each of these data sets.

Looking into our best-fit fitting parameters, we note a few key results. First, the slope of DS1 (2.95 ± 0.41) is shallower than the slopes found for the other data sets (DS2: 3.21 ± 0.66, DS3: 3.44 ± 0.48, and DS4: 3.09 ± 0.39). This result again implies that the BLR extinction might be somewhat responsible for flattening the slope. However, we cannot statistically confirm this, since uncertainties in the slopes are quite large for our data sets. Second, the range of slopes derived for our BASS sample, $2.54 \leqslant \beta \leqslant 3.92$ is consistent with what is found in previous studies. Specifically, our results are consistent with those presented by C20, which reports a slope of $\beta = 3.38 \pm 0.65$, an intercept of $\alpha = 8.14 \pm 0.20$ and an intrinsic scatter of $\epsilon = 0.32 \pm 0.06$ for the LLAMA sample. Our slopes are also consistent with the slope reported by Woo et al. (2013) for a sample with RM measurements (3.46 ± 0.61). On the other hand, the slope of 4.38 ± 0.29 reported by KH13 is not consistent with the slopes of our data sets. Moreover, none of the slopes we derive is consistent with the steep slope of 5.64 ± 0.32 reported by MM13 (which included bright central cluster galaxies). The more recent study by Bennert et al. (2021) reported a slope of 3.89 ± 0.53 for 29 RM AGNs and a slope of 4.55 ± 0.29 for 51 inactive galaxies. Compared with these, our results for the BASS AGNs are consistent with the RM AGN sample of Bennert et al. (2021) slope (within uncertainties) but are inconsistent with the slope found for inactive galaxies. Thus, our analysis strengthens the evidence that AGNs show a shallower $M_{BH}-\sigma_\star$ relation compared to inactive galaxies.

In Figure 3, we present the best-fitting $M_{BH}-\sigma_\star$ relations for the DS1 and DS4 data sets (along with the corresponding $\pm 2\sigma$ confidence ranges (also see Appendix F). Additionally, we compare our results with other $M_{BH}-\sigma_\star$ relations reported by KH13 and MM13. A significant fraction of AGNs is found to be below the canonical $M_{BH}-\sigma_\star$ relation reported by KH13. This discrepancy appears to increase as the extinction in broad-line regions (BLRs) increases, which is discussed further in Section 4.4.1. The presence of shallower slopes and large

scatter in the low-mass end of the M_{BH}–$\sigma_\star$ relation can be seen from the figure; therefore, this further pushes us to discuss the fundamental differences between AGNs and inactive galaxy samples causing this discrepancy.

4.3. Understanding the Differences between AGNs and Inactive Galaxies

We have demonstrated that our sample of Type 1 AGNs shows significantly shallower M_{BH}–$\sigma_\star$ slopes relative to the canonical relation determined for inactive galaxies. This may be driven by multiple effects, related both to (host) galaxy evolution and BLR structure, as discussed below.

First, one can postulate that AGNs must follow the same M_{BH}–$\sigma_\star$ relation as inactive galaxies, in which case the observed discrepancy may be attributed to variations in the BLR geometry (Onken et al. 2004). We recall that efforts to obtain an average f factor have been limited to only a few dozen AGNs with a relatively narrow range of M_{BH} and $\log \lambda_{Edd}$.

Moreover, some studies suggest that the BLR geometry (i.e., as encoded in the f factor) may depend on some fundamental BH properties, including both observed trends between f and FWHM, M_{BH} and/or $\log \lambda_{Edd}$ (e.g., Storchi-Bergmann et al. 2017; Mejía-Restrepo et al. 2018a, and references therein), and disk-wind models that anticipate such trends (e.g., Proga & Kallman 2004).

Second, since M_{BH} is estimated by different methods for AGNs and inactive galaxies, different selection effects and biases may affect these two kinds of samples. As discussed by Bernardi et al. (2007); Shankar et al. (2016), a resolution-dependent bias affects dynamical M_{BH} determinations in inactive galaxies, which does not affect AGNs.[34] On the other hand, the RM AGN samples based on which the best M_{BH} measurements are obtained, and the SE method is based, may also be biased. In particular, most RM efforts have been focused on low-redshift, low-to-medium luminosity AGNs, where sufficient variability can be expected and where emission line time lags can be more robustly monitored (but see exceptions in, e.g., Lira et al. 2018). In addition to the challenge of measuring $\sigma_\star$, and thus inferring the M_{BH} scaling (f) in such luminous sources (e.g., Grier et al. 2013), it is also possible that such AGNs may not be representative of highly luminous AGNs like those probed by BASS or by high-redshift surveys (see detailed discussion of luminosity-related biases in, e.g., Shen et al. 2008). These difficulties add to other issues concerning which broad emission line, and which line profile measurement, best probe the virialized BLR motion (e.g., see Peterson et al. 2004; Collin et al. 2006; Dalla Bontà et al. 2020), how to inter-calibrate SE prescriptions based on various emission lines (e.g., Shen & Liu 2012; Park et al. 2017; Mejía-Restrepo et al. 2018a, 2018b; Dalla Bontà et al. 2020), as well as BLR extinction (as shown in this paper).

Third, significant differences in the kind of SMBHs probed through our AGN sample and the literature inactive galaxy sample, as reflected in their different M_{BH} distributions, might also play a role in the slope discrepancy. The extinction-uncorrected M_{BH} estimates for our AGN sample cover the range of $5 \lesssim \log(M_{BH}/M_\odot) \lesssim 8.9$, with a median value of ≈ 7.5. However, an important fraction of the inactive galaxy sample (35% of the total KH13 sample) consists of SMBHs

with $\log(M_{BH}/M_\odot) > 9$. On the other hand, 31 of our AGNs (20%) are found to have $\log(M_{BH}/M_\odot) \lesssim 7$, compared with only two such SMBHs (4%) among the KH13 sample of inactive galaxies (see Bennert et al. 2021, for more details). Thus, the high-mass regime is significantly overrepresented by the inactive galaxies sample with $\sigma_\star$ measurements (or, alternatively, underrepresented in our AGN sample; see Ananna et al. (2022) for a detailed census of M_{BH} distributions among BAT AGNs). The lack of $\sigma_\star$ measurements in the high-M_{BH} regime might flatten the slope of the relation for AGN samples, whereas it might result in a steeper relation for inactive galaxy samples if those lack low-M_{BH} systems. The latter may reflect, again, known biases in our current ability to measure $\sigma_\star$ in inactive galaxies in the local Universe (see above).

The differences in M_{BH} distributions between the active and inactive galaxy samples could also reflect deeper differences in the evolutionary paths experienced by the two galaxy populations. In this context, we note that the majority of elliptical, inactive galaxies (or those with classical bulges) are thought to be the result of a previous major merger (see, e.g., Kormendy & Kennicutt 2004; Kormendy & Ho 2013), while disk-dominated galaxies, or galaxies with pseudo-bulges and/or bars, are thought to be dominated by secular evolution. Such galaxies typically host lower-mass SMBHs, and were shown to present significantly larger scatter, and shallower slopes, for their M_{BH}–$\sigma_\star$ relations (e.g., Graham 2008; Hu 2008; Greene et al. 2010; Ho & Kim 2014). Combined with our findings, it is thus possible that our AGN hosting galaxies tend to be disk dominated, or to have pseudo-bulges (and/or bars), and to mark evolutionary paths that are different than those of large elliptical (or bulge-dominated) galaxies (see Koss et al. 2011 for additional evidence for disk dominance among BAT-selected AGNs).

Finally, we note two more subtle issues when considering the M_{BH}–$\sigma_\star$ relations of active and inactive galaxies. From a theoretical perspective, the growth of SMBHs and of the bulges that host them does not have to be perfectly synchronized (e.g., Ho 2005; Kim et al. 2006; Volonteri 2012; Ricarte et al. 2019), which will introduce additional scatter in the M_{BH}–$\sigma_\star$ relation. Specifically for our findings, as we are focusing on rather powerful AGNs, the SMBHs are experiencing a significant growth episode, which might not be echoed by a corresponding $\sigma_\star$ increase, thus leading to an expectation for the systems to grow *toward* the canonical M_{BH}–$\sigma_\star$ relation (in the near cosmic future; see also Section 4.4.4). From a practical perspective, host galaxy disk contamination can increase the observed $\sigma_\star$ by up to $\approx 25\%$ (due to orientation and/or rotation; see, e.g., Kang et al. (2013), Bellovary et al. (2014), Eun et al. (2017), and C20). In addition, as suggested by Debattista et al. (2013), the compression of bulge caused by the disk formation might introduce an increase of 10% in $\sigma_\star$. Therefore, the increased $\sigma_\star$ might cause additional offsets in the M_{BH}–$\sigma_\star$ relation for galaxies hosting disks.

4.4. Offset from the M_{BH}–$\sigma_\star$ Relation

4.4.1. Extinction in the BLR

Next, we look into the BLR extinction, as can be determined from the suppression of broad Hα line emission for any given ultra-hard X-ray luminosity. Assuming such suppression is caused entirely by dust extinction, and that the gas-to-dust ratio

---

[34] See also van den Bosch et al. (2015) for further discussion of possible biases regarding inactive galaxies.
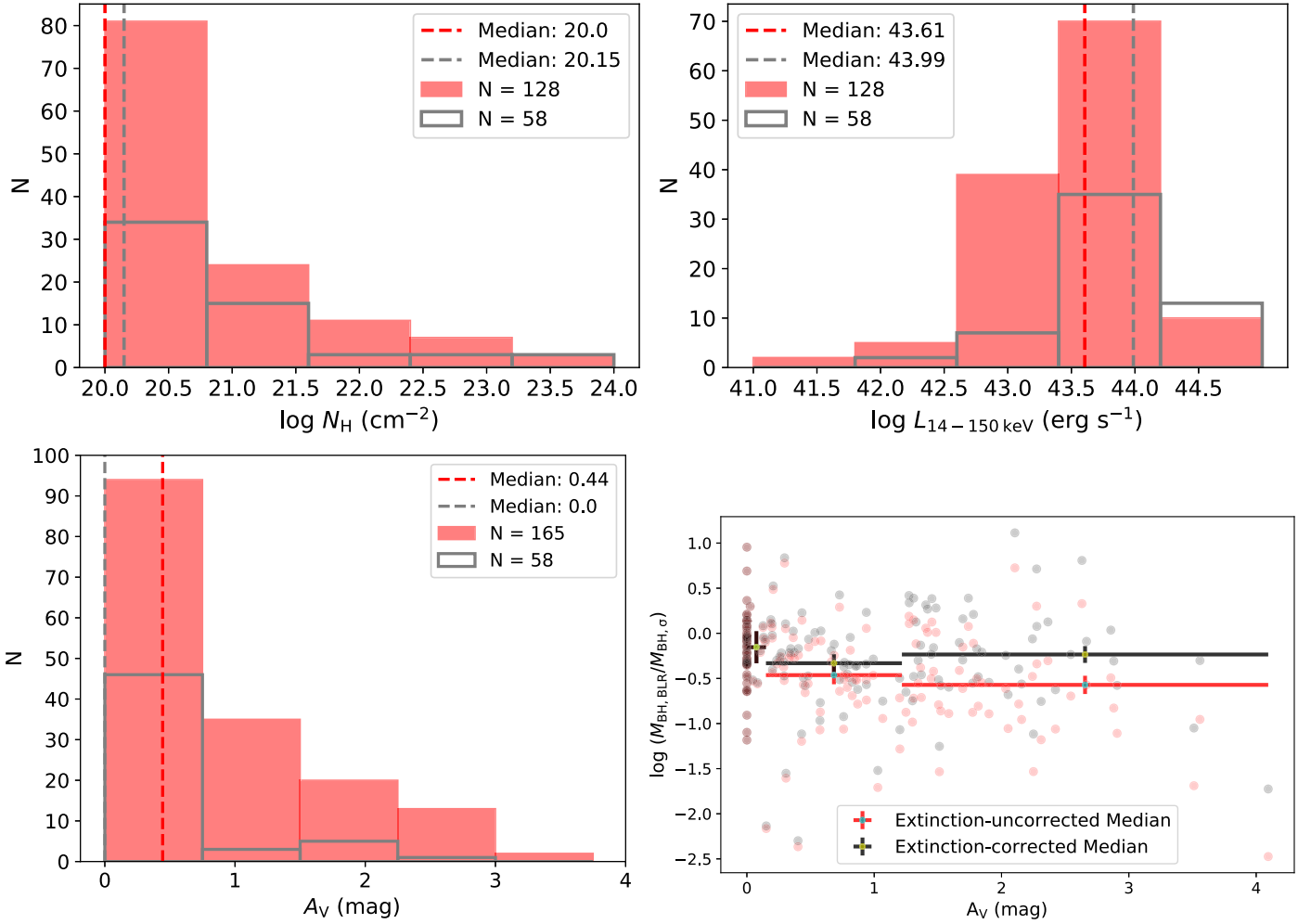
Figure 4. The distribution of hydrogen column density (top left), hard X-ray luminosity (top right) and the extinction in the BLR (bottom left). The red columns represent the presented parameter's distribution for AGNs with successful $\sigma_\star$ fits, whereas the gray ones represent the ones with failed $\sigma_\star$ fits. Median values are presented as red and gray dashed vertical lines, respectively. Bottom right: the offset from the $M_{\rm BH}-\sigma_\star$ relation vs. the extinction in the BLR for our sample of AGNs. The medians (together with the bin edges and the standard error on the median) are presented for three bins with equal numbers of data points.

is similar to that of the Milky Way, i.e., yielding $N_{\rm H}/A_{\rm V} = 1.79$–$2.69 \times 10^{21}$ cm^{-2} (Predehl & Schmitt 1995; Nowak et al. 2012), we expect a maximum $N_{\rm H}$ threshold of $\approx 10^{22.3}$ cm^{-2} for Type 1 AGNs (i.e., excluding Sy 1.9s with broad Hα emission lines) for discriminating X-ray absorbed and unabsorbed sources as described by Burtscher et al. (2016). We note that there are only 10 absorbed AGNs in our sample (see the top-left panel of Figure 4). The median $\log(N_{\rm H}/\rm cm^{-2})$ values for our AGNs with successful and failed $\sigma_\star$ fits are 20.0 and 20.15, respectively. The majority of our $N_{\rm H}$ estimates cluster around $\log(N_{\rm H}/\rm cm^{-2}) = 20.0$. This value is the upper limit due to Galactic extinction placed by Ricci et al. (2017b) for completely unobscured sources, since lower intrinsic $N_{\rm H}$ values cannot easily be determined. We also stress that we have no Compton-thick sources $(\log[N_{\rm H}/\rm cm^{-2}] > 24)$ in our sample.

We can thus use the $\log(L_{14-150\,\rm keV}^{\rm int}/\rm erg\,s^{-1})$ as a probe of the extinction-corrected broad Hα luminosities ($L_{\rm H\alpha}^{\rm corr}$). In the top-right panel of Figure 4, we report the distribution of $\log(L_{14-150\,\rm keV}^{\rm int}/\rm erg\,s^{-1})$ for AGNs with successful and failed $\sigma_\star$ fits resulting in the median values are 43.61 and 43.99, respectively. The difference between the observed and intrinsic Hα luminosities, accordingly, gives us the X-ray-derived Hα

extinction ($A_{\rm H\alpha}$) for the BLR (see Equations (2) and (3)). We note that applying such conversion introduces an average uncertainty of 0.4 dex in $L_{\rm H\alpha}$ estimations (Shimizu et al. 2018). The bottom-left panel of Figure 4 shows the distribution of $A_{\rm V}$ derived through our approach, which has median and mean $A_{\rm V}$ (see Equation (4) for the conversion between $A_{\rm V}$ and $A_{\rm H\alpha}$) values of 0.44 and 0.84 mag, respectively. Importantly, a significant fraction (66%) of our AGNs has $A_{\rm V} < 1$ mag. We also stress that there are only 22 AGN with $A_{\rm V} > 2$ mag. We note that extinction correction has a very large uncertainty for highly extincted sources, and thus should be used with great caution. Finally, we suggest using near-infrared broad emission lines for such extreme cases (Ricci et al. 2022).

In the bottom-right panel of Figure 4, we present the offset of our AGNs from the canonical $M_{\rm BH}-\sigma_\star$ relation of KH13, which was defined as $\Delta\mathcal{M}_{\rm BH} \equiv \log(M_{\rm BH,BLR}/M_{\rm BH,\sigma})$ in the introduction, versus the BLR extinction estimates. We plot these for both the extinction-uncorrected and extinction-corrected data sets. Despite the significant scatter in this parameter space diagram, we find a statistically significant anticorrelation, as supported by a formal Spearman correlation test ($\rho = -0.38 \pm 0.07$, $p \ll 0.01$) showing that the extinction in the BLR plays a role in the offset. Applying the extinction correction reduces $\Delta\mathcal{M}_{\rm BH}$ to some extent, but $\Delta\mathcal{M}_{\rm BH}$ persists across all extinction regimes (see binned data
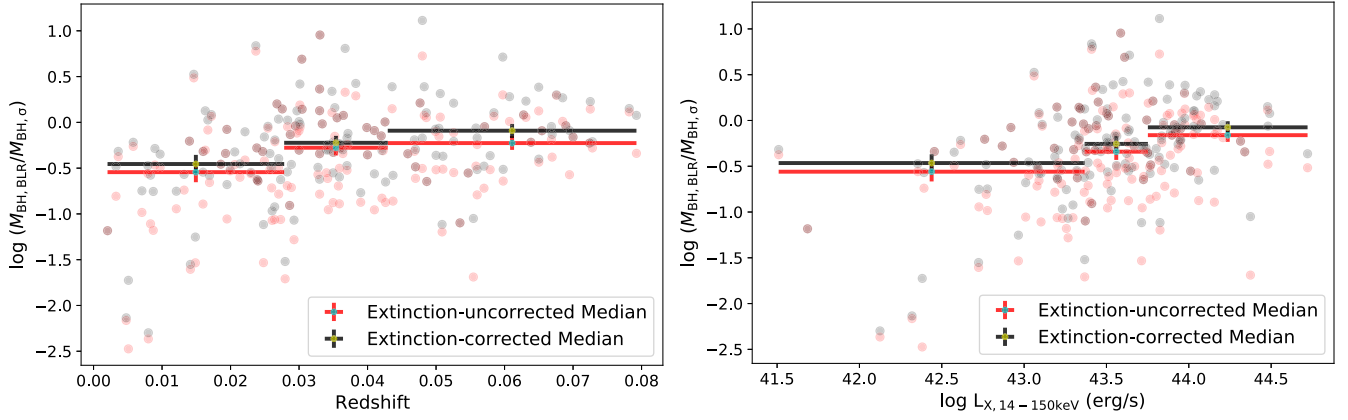
Figure 5. Left: comparison between $\Delta\mathcal{M}_{BH}$ and redshift. Right: comparison between the offset from the M_{BH}–$\sigma_\star$ relation and hard X-ray luminosity. The medians (together with the bin edges and the standard error on the median) are presented for three bins with equal numbers of data points.

points in Figure 4). This result is a confirmation of the findings by C20, which used a significantly smaller sample of Swift-BAT detected AGNs with a redshift cutoff of $z < 0.01$ and an ultra-hard X-ray luminosity cutoff of $\log(L_{14-195\,keV}/erg\,s^{-1}) \geqslant 42.5$.

We emphasize that applying the (uncertain) extinction correction may introduce significant additional uncertainty to M_{BH} estimates (through its dependence on $L_{H\alpha}$), for two reasons. First, the extinction corrections themselves are somewhat uncertain. Second, the potential flux variability between the BAT X-ray measurements and the optical spectroscopy can cause an overcorrection by up to ∼1 dex for some sources. To demonstrate the scope and challenges of the extinction corrections, we consider the individual case of NGC 1365 (BAT 184). The observed broad Hα luminosity for this source is $\log(L_{H\alpha}^{obs}/erg\,s^{-1}) = 39.37$ and the extinction we derive is $A_{H\alpha} = 3.40$ mag, yielding an extinction-corrected line luminosity of $\log(L_{H\alpha}^{corr}/erg\,s^{-1}) = 40.73$, i.e., an upward correction of 1.36 dex. Correspondingly, the extinction-corrected M_{BH} differs from the raw M_{BH} estimate (i.e., Equation (1)) by 0.75 dex. Here, we note that NGC 1365 is a well-known changing look AGN (e.g., Risaliti et al. 2000, 2009; Walton et al. 2014; Mondal et al. 2022; Ricci & Trakhtenbrot 2022; Temple et al. 2022); therefore, the variability can be somewhat responsible for this discrepancy for such sources.

As shown throughout this paper, we claim that the extinction in the BLR can cause considerable underestimation of M_{BH} for highly obscured AGNs unless it is taken into account. This result is also shown by C20 and recent BASS studies (Mejía-Restrepo et al. 2022; Ricci et al. 2022). However, applying extinction correction increases the noise in data. Therefore, as proposed by Ricci et al. (2022), we encourage measuring black hole masses using near-infrared broad emission lines, which are expected to be less affected by dust extinction.

4.4.2. Redshift and Intrinsic X-Ray Luminosity

In Figure 5, we present a direct comparison between $\Delta\mathcal{M}_{BH}$ and both z (left panel) and $\log(L_{14-150\,keV}^{int}/erg\,s^{-1})$ (right panel), for both extinction-corrected and uncorrected measurements. We see trends of increasing $\Delta\mathcal{M}_{BH}$ with both increasing redshift and luminosity, regardless of the extinction correction. For the trend with redshift, a Spearman test results in correlation coefficients of $\rho = 0.33 \pm 0.03$ and 0.36 ± 0.04 for the extinction-uncorrected and extinction-corrected data, respectively (with $p \ll 0.01$ for both cases). For the trend with

X-ray luminosity, the corresponding correlations are $\rho = 0.32 \pm 0.03$ and 0.38 ± 0.04 (with $p \ll 0.01$ for both cases). Although each of these trends is statistically significant, they are very likely interleaved given the flux-limited nature of the BAT survey. There are two-sided biases here: (1) as redshift increases, the chance of detecting lower luminosity sources by X-ray instruments decreases, (2) the number of X-ray bright AGNs are limited in the nearby universe (e.g., Davies et al. 2015; Caglar & Hudaverdi 2017). In fact, $L_{H\beta}$, L_{5100}, and $L_{H\alpha}$ are strongly correlated with $\log(1 + z)$ ($\rho = 0.51 \pm 0.03$, 0.54 ± 0.03, and 0.66 ± 0.02, respectively,) which indicates a strong redshift-luminosity selection bias. We also point out that some contribution to this trend might come from projection effects caused by the limitation of instrumental aperture sizes since the M_{BH}–$\sigma_\star$ relation is assumed to hold at effective radii (see the discussion in Appendix G). The M_{BH} estimates from the BLR are not affected by such limitations, since BLR gas resides at sub-parsec scales.

4.4.3. Impact of the M_{BH}–$\sigma_\star$ Relation Used

The slope of the M_{BH}–$\sigma_\star$ relation may be indicative of the physics behind the AGN-driven feedback mechanism. Specifically, $M_{BH} \propto \sigma^4$ corresponds to momentum-driven feedback while $M_{BH} \propto \sigma^5$ corresponds to energy-driven feedback (e.g., Silk & Rees 1998; King 2003). Previous efforts to determine a (universal) M_{BH}–$\sigma_\star$ relation yielded a wide range of slopes, i.e., $\beta \simeq 3.7$–5.6 for inactive galaxies (e.g., Ferrarese & Merritt 2000; Gebhardt et al. 2000; Tremaine et al. 2002; Gültekin et al. 2009; Beifiori et al. 2012; Batiste et al. 2017) and $\beta \simeq 3.4$–4.0 for AGNs (e.g., Woo et al. 2013, 2015). Although most of these studies report a tight relation, with an intrinsic scatter of $\gtrsim 0.3$ dex, the uncertainties on the slope typically exceed $\Delta\beta \simeq 0.3$. AGN samples tend to show both larger uncertainties (due to their smaller size) and flatter slopes (see also, Shen et al. (2015). Adopting different M_{BH}–$\sigma_\star$ relations naturally results in additional differences in M_{BH}, ranging from ∼0.35 dex for a fiducial $\sigma_\star = 150\,km\,s^{-1}$ to over 0.8 dex for the lower and higher ends of the $\sigma_\star$ (or M_{BH}) distribution.

In the left panel of Figure 6, we plot M_{BH} estimates for our BASS sample obtained from three different scaling relations (C20; KH13, and MM13) versus the corresponding $\Delta\mathcal{M}_{BH}$ (the difference between the extinction-corrected M_{BH} estimates versus the ones from the adopted $M_{BH} - \sigma_\star$ relation). We note
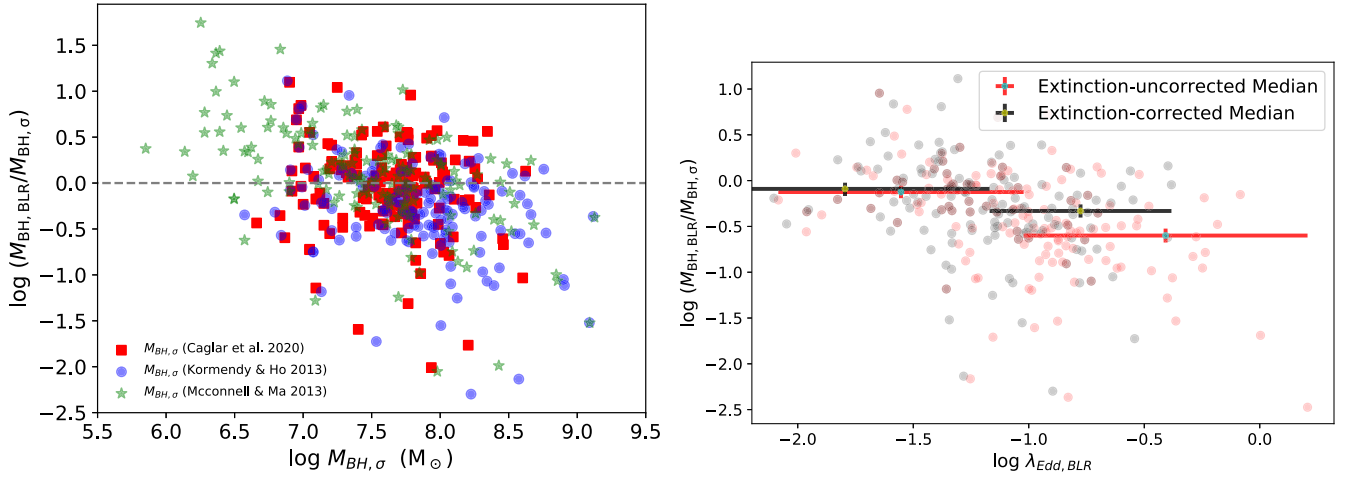
Figure 6. Comparison between the adopted M_{BH}–$\sigma_\star$ relation as an estimator of M_{BH} (left). The $\Delta\mathcal{M}_{BH}$ vs. Eddington ratio (right). The medians (together with the bin edges and the standard error on the median) are presented for two bins with equal numbers of data points.

that these three calibrations were derived using different samples of different types of galaxies: the KH13 relation is based on elliptical and classical bulge galaxies, whereas the MM13 sample consists of early and late-type galaxies, as well as BCGs. On the other hand, the C20 sample consists of luminous, hard X-ray-selected local Type 1 AGNs. It appears that black hole masses obtained using the M_{BH}–σ relation reported by C20 are relatively closer to the zero-point (with a median offset of 0.03 ± 0.04 dex) compared to the ones reported by KH13 (with a median offset of -0.24 ± 0.05 dex) and MM13 (with a median offset of 0.11 ± 0.05 dex). Using our sample of AGNs, we report that the scaling relation by KH13 shows a tendency to overestimate black hole masses, whereas the scaling relation by MM13 tends to underestimate black hole masses. On the other hand, the C20 version of the M_{BH}–σ relation provides a better description of the BASS data set. This result indicates that AGNs might be following a different M_{BH}–$\sigma_\star$ relation.

4.4.4. The Eddington Ratio and Accretion Rates

In this section, we investigate whether $\Delta\mathcal{M}_{BH}$ is correlated with the Eddington ratio. We first note that the extinction-uncorrected Eddington ratio estimates for our sample are in the range of $-2.10 < \log \lambda_{Edd} < 0.21$, with a median value of $\log \lambda_{Edd} \simeq -1$. Only two sources have $\log \lambda_{Edd} > 0$ (NGC 1365 and PKS0521-36); however, both have high BLR extinction ($A_V > 3.5$ mag), and thus their M_{BH} are underestimated, and accordingly, their $\log \lambda_{Edd}$ are overestimated. If we exclude high-A_V sources (with $A_V > 1$ mag), we only have five AGNs exceeding $\log \lambda_{Edd} > -0.5$. (Mrk 359, Mrk 382, Mrk 783, 2MASXJ08551746-2854218, and 2MASXJ21344509-2725557). After applying the BLR extinction correction, the extinction-corrected Eddington ratio estimates are in the range of $-2.43 < \log \lambda_{Edd,corr} < -0.37$, with a median $\log \lambda_{Edd,corr} = -1.16$.

In the right panel of Figure 6, we plot $\Delta\mathcal{M}_{BH}$ versus the $\log \lambda_{Edd}$, including both extinction-corrected and uncorrected sets of estimates (affecting both axes). The BLR extinction correction causes the M_{BH} estimates to increase, and the $\log \lambda_{Edd}$ estimates to accordingly decrease, by ~ 0.1 dex (on average). However, for AGNs with high levels of BLR extinction ($A_V > 2$ mag), the raw $\log \lambda_{Edd}$ can be overestimated

by ~ 0.4 dex. For the most extreme case in our sample, NGC 1365 (BAT ID 184; $A_V = 4.1$ mag) the change in $\log \lambda_{Edd}$ is 0.75 dex. To investigate trends in this parameter space, we first divide the data points into two bins in Eddington ratio, low and high, with equal numbers of data points in each. We see that the median $\log \lambda_{Edd}$ values show a decreasing trend for both extinction-corrected and uncorrected estimates. This trend is then also confirmed through a formal Spearman correlation test (for all extinction-corrected data points), which results in $\rho = -0.37 \pm 0.05$ ($p \ll 0.01$).

We now discuss the possibility of whether AGNs in the nearby universe are growing toward the M_{BH}–$\sigma_\star$ relation. To understand this, we first estimate the physical accretion rates of our AGNs, assuming $L_{bol} = \eta \dot{M} c^2$ and a universal radiative efficiency $\eta = 0.1$. The resulting accretion rates are in the range of $10^{-4} \leqslant \dot{M} \leqslant 1.4\ M_\odot\ \mathrm{yr}^{-1}$ with a median of $\dot{M} = 0.085\ M_\odot\ \mathrm{yr}^{-1}$. Most of our Type 1 BASS AGNs are thus growing with low accretion rates and at sub-Eddington levels. Here, if we assume that the offset of our sources from the canonical M_{BH}–$\sigma_\star$ relation is explained by the ongoing growth of SMBHs destined to *catch up* with their host galaxies, we can actually estimate the required duration of the active accretion (i.e., AGN) phase for achieving this. For our BASS-based sample, the median M_{BH} is $\sim 10^{7.5}\ M_\odot$ and the average $\Delta\mathcal{M}_{BH}$ is 0.3 dex, which for the scenario we consider here would imply the SMBHs have to grow by a factor of ~ 2, or by $\sim 10^{7.5}\ M_\odot$ in mass. Given the aforementioned median accretion rate of $0.085\ M_\odot\ \mathrm{y}^{-1}$, this yields an SMBH growth time (AGN phase) of $\sim 10^{8.5}$ yr (i.e., ~ 0.4 Gyr) is needed for eliminating the offset between BH mass estimates from $M_{BH,BLR}$ and $M_{BH,M-\sigma_\star}$. On one hand, this rough estimate for the AGN lifetime is consistent with that is implied from the integrated accretion density of distant AGNs by previous works (10^{7-9} yr; i.e., the Soltan argument; Soltan 1982; Martini & Weinberg 2001; Marconi et al. 2004). On the other hand, more recent evidence for the episodic nature of AGN accretion, with luminous episodes lasting as little as $\sim 10^5$ yr (or even less; see, e.g., Schawinski et al. 2015; Shen 2021, and references therein), means that closing the BH mass gap through persistent growth at the observed (low) accretion rates is very unlikely. Of course, SMBHs are expected to undergo a wide range of accretion rates, from sub-Eddington to super-Eddington levels,

4.5. Correlation Matrices of the Observable Parameters

In the preceding sections, we have directly addressed several potential correlations between $\Delta\mathcal{M}_{BH}$, which by itself is derived from the AGN luminosity, broad-line width, and $\sigma_\star$ and key AGN properties. Our analysis revealed some statistically significant trends and refuted others, while facing several observational biases. This motivates us to assess more systematically which basic observables and derived quantities are correlated with each other.

To this end, we compute the correlation matrix for the following quantities: $\sigma_\star$ $\log(1 + z)$, $FWHM_{H\beta}$, $L_{H\beta}$, $M_{BH,H\beta}$, $FWHM_{H\alpha}$, $L_{H\alpha}$, $M_{BH,H\alpha}$, N_H, A_V, L_{bol}, λ_{Edd}, and $\Delta\mathcal{M}_{BH}$. Here, we note that all quantities mentioned in the previous sentence are used with their raw observed values and no extinction correction was applied to them. In Table 4 (in Appendix H), we present the correlation matrix computed using the Spearman rank-order correlation test. We use three different colors to indicate the significance of the correlation (or lack thereof): black and blue numbers represent significant correlations, with $p \ll 0.01$ and < 0.05, respectively, while red numbers represent null results (i.e., lack of a significant correlation), with $p \gg 0.1$. For example, both the $FWHM_{H\alpha}$ and $M_{BH,H\alpha}$ pair of parameters, or the $L_{H\beta}$ and $L_{H\alpha}$ pair, show strong correlations ($\rho = 0.79 \pm 0.02$ and 0.85 ± 0.01, respectively; both with $p \ll 0.01$). These example results are not surprising given that the parameters in both comparisons are, by definition, closely interlinked.

The BLR extinction (A_V) shows a statistically significant ($p \ll 0.01$) anticorrelation with $L_{H\beta}$, L_{5100}, $L_{H\alpha}$, and $\Delta\mathcal{M}_{BH}$ (with $\rho = -0.49 \pm 0.03$, -0.43 ± 0.03, -0.50 ± 0.03, and -0.38 ± 0.07, respectively), while on the other hand showing a significant correlation with $\log\lambda_{Edd}$ ($\rho = 0.42 \pm 0.05$, $p \ll 0.01$). We also see that many properties are correlated with redshift, including $L_{H\beta}$, L_{5100}, $L_{H\alpha}$, L_{bol} and $\Delta\mathcal{M}_{BH}$ ($\rho = 0.51 \pm 0.03$, 0.54 ± 0.03, 0.66 ± 0.02, 0.83 ± 0.05, and 0.33 ± 0.03 respectively; all with $p \ll 0.01$). As discussed above, the correlations between redshift and the various luminosities are a manifestation of the flux-limited nature of our parent sample from the survey. We can finally also see the anticorrelation between $\Delta\mathcal{M}_{BH}$ and both λ_{Edd} and A_V, which was also discussed above. In Appendix I, we present the principal component analysis (PCA) results in order to identify the main parameters driving the variance in our data sets (see Table 5).

5. Conclusion

We presented a study of stellar velocity dispersions ($\sigma_\star$) in the host galaxies of a large sample of broad-line (Type 1), ultra-hard X-ray selected low-redshift AGNs. Our $z \leqslant 0.08$ AGNs are drawn from the flux-limited 105 month Swift-BAT catalog, and our analysis relies on optical spectroscopy obtained as part of the BASS project. We provide new measurements of $\sigma_\star$, obtained for both the CaT and the Ca H+K+Mg I spectral complexes, for a total number of 173 AGNs. This work is one of the largest $\sigma_\star$ investigations for Type 1 AGNs. Using the broad emission line measurements and derived M_{BH} estimates made available through BASS/DR2 (Mejía-Restrepo et al. 2022), we compare our results with the established M_{BH}–$\sigma_\star$ relations. Our main findings are as follows:

1. The average offset between σ_{blue} and σ_{red} measurements is essentially negligible, at 0.002 ± 0.001 dex, and this shows that these two distinct spectral regimes provide highly consistent $\sigma_\star$ measurements.

2. We fit new M_{BH}–$\sigma_\star$ relations using various data sets based on our sample and measurements. The slopes we find are significantly shallower than those reported in the literature for inactive galaxies. This result agrees with, and strengthens, the conclusion of previous studies of broad-line, low-redshift AGNs. Using an appropriate, AGN-based M_{BH}–$\sigma_\star$ relation for SE prescriptions may thus be advisable.

3. We show that BLR extinction plays an important role in SE or virial M_{BH} estimates, in that it causes the underestimation of M_{BH} and—consequentially—the overestimation of the Eddington ratios ($\log\lambda_{Edd}$).

4. We have looked into differences between SE and $\sigma_\star$-based M_{BH} estimates, $\Delta\mathcal{M}_{BH}$, where the latter are based on the canonical M_{BH}–$\sigma_\star$ relation of KH13. We found that $\Delta\mathcal{M}_{BH}$ shows statistically significant correlations with both redshift and luminosity; however, these trends are likely driven by the nature of the survey and are mutually degenerate.

5. After applying the extinction correction to M_{BH} measurements, we find Eddington ratios in the range of $-2.43 < \log\lambda_{Edd,corr} < -0.37$. In addition, the resulting physical accretion rates (ranging $10^{-4} \lesssim \dot{M} \lesssim 1.40$ $M_\odot$ yr^{-1}) suggest that our broad-line BASS AGNs are growing at sub-Eddington levels.

The implications of our analysis are not yet fully understood, and further research is necessary to gain a clearer understanding of all biases and discrepancies between AGN and inactive galaxy samples. We specifically foresee further observations with high-resolution instruments, aboard the Hubble Space Telescope and/or JWST, to directly probe how different types of host galaxy morphology might affect our interpretation of the M_{BH}–$\sigma_\star$ relations for powerful AGNs. Additionally, more black hole mass measurements using near-infrared spectroscopy could help reduce the effects caused by dust, which can significantly interfere with our current understanding of AGN populations and of their relationship with their host properties (as we have demonstrated here). The results presented in this work thus aim to serve as a reference point for forthcoming, more detailed studies of the M_{BH}–$\sigma_\star$ relation.

While the large size and high completeness of the sample used for our analysis present significant progress in studying the M_{BH}–$\sigma_\star$ relation, and extinction effects, in low-redshift AGNs, it also highlights areas where more progress in terms of the census of low-redshift AGNs and their hosts is direly needed. Specifically, new and upcoming X-ray missions, such as the extended Roentgen Survey with an Imaging Telescope Array on board the Spectrum-Roentgen-Gamma (Predehl et al. 2021), Advanced Telescope for High Energy Astrophysics (Nandra et al. 2013), and the Advanced X-ray Imaging Satellite (Mushotzky 2018), will greatly improve our ability to construct yet larger, more complete AGN samples at high redshift for which homogeneous and robust spectral analysis can be obtained, to deduce key properties both in the X-ray and also

Caglar et al.

in optical regimes thanks to spectroscopic surveys such as SDSS-V (Kollmeier et al. 2017; Almeida et al. 2023) or the 4 m Multi-Object Spectroscopic Telescope (de Jong et al. 2016). This will further help to break any outstanding degeneracies between AGN luminosities, BH masses, accretion rates and states, and host galaxy types and properties.
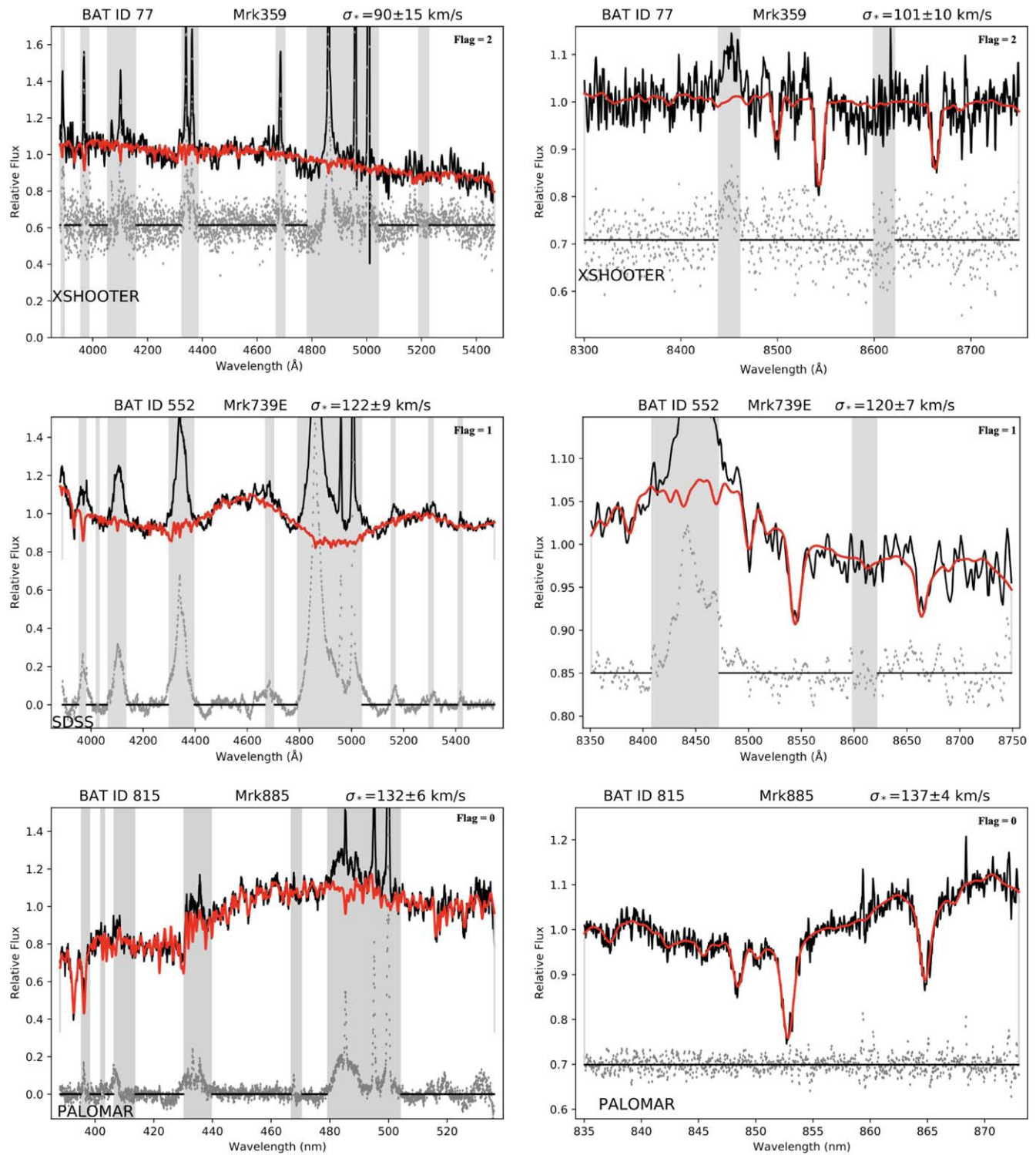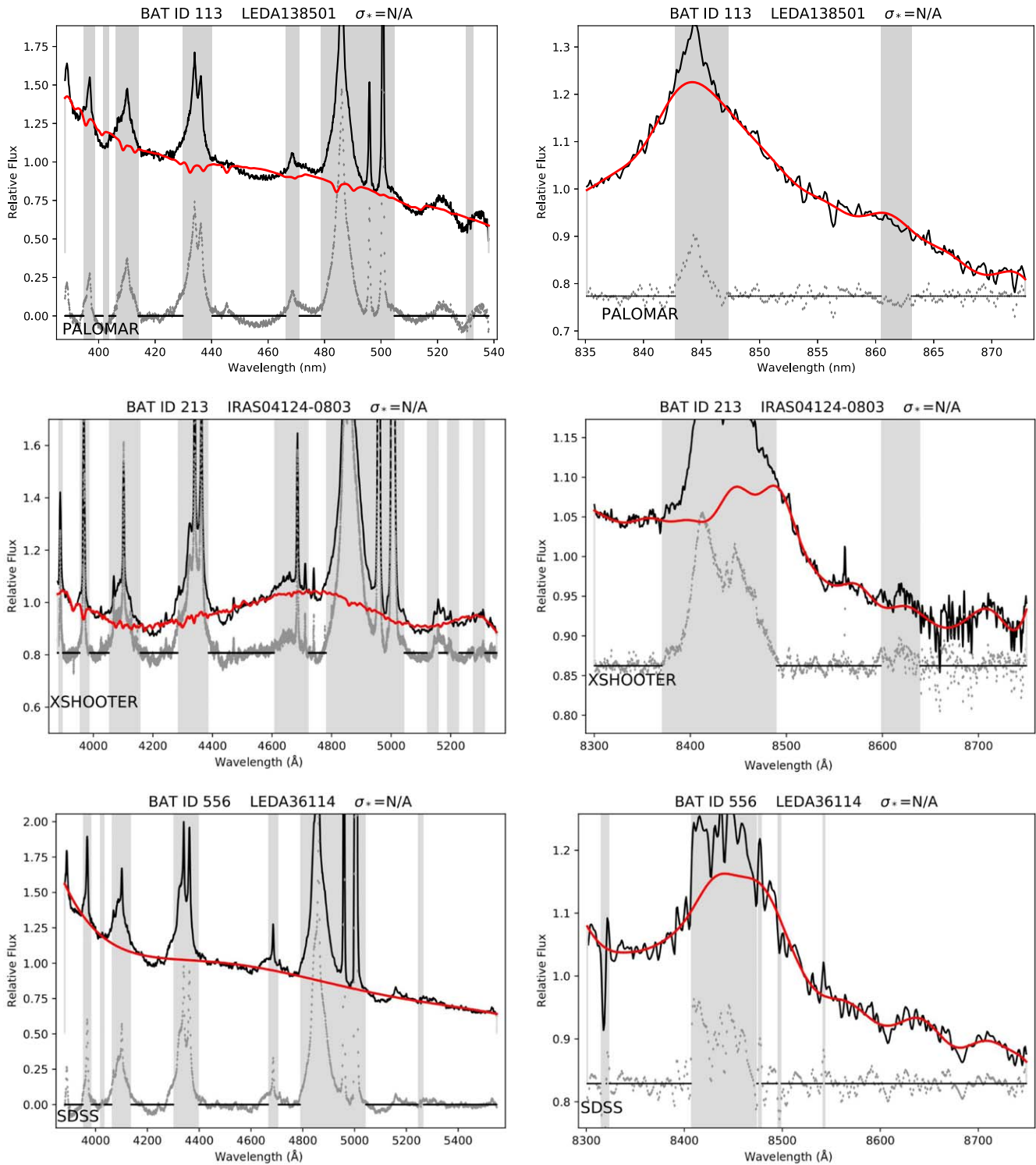
Appendix A
pPXF Fit Results

In Figure 7(a), we present three examples of successful spectral fits, yielding robust measurements of σ_{blue} (left column) and σ_{red} (right column). We also show three examples of failed spectral fits in Figure 7(b) (again, for both σ_{blue} and σ_{red}). In both cases, the examples shown are representative of our spectral setups and fitting results.

Figure 7. (a) Examples of the successful σ_{blue} (left panels) and σ_{red} (right panels) fitting plots for SDSS, VLT/X-shooter, and Palomar/Double Spectrograph data (from top to bottom). (b) Examples of the failed σ_{blue} (left panels) and σ_{red} (right panels) fitting plots for Palomar/Double Spectrograph, VLT/X-shooter, and SDSS data (from top to bottom). The complete figure set (539 images) of successful and failed sources is available in the online journal.

(The complete figure set (539 images) is available.)

(b)

Figure 7. (Continued.)

Appendix B
Comparison of $\sigma_\star$ Measurements from Different Instruments in Our Survey

For a small subset of AGNs in our sample, where more than one optical spectrum is available, we were able to obtain (at least) two independent measurements of $\sigma_\star$ from the same

spectral region. In Figure 8, we present a pair-wise comparison of these duplicate $\sigma_\star$ measurements. We find that our duplicate $\sigma_\star$ measurements, obtained with different instruments, are highly consistent with each other, for both σ_{blue} and σ_{red} measurements (i.e., both spectral regimes considered here). There is only one significant outlier from the 1:1 line in
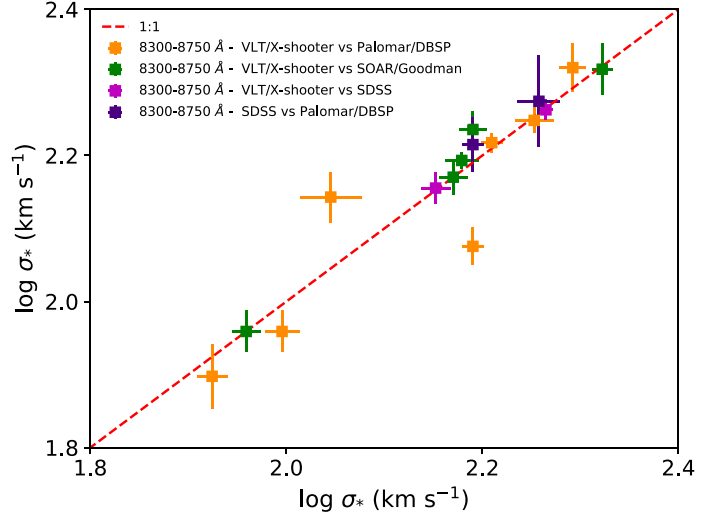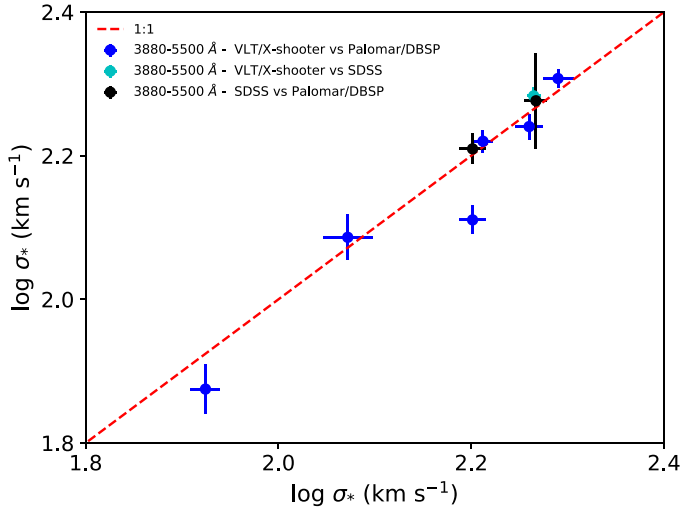
Figure 8. Left: comparison of $\sigma_\star$ measurements between the instruments used in this study for the 3880–5500 Å region. Right: same as the bottom-left figure, but for the 8350–8750 Å region. The red dashed lines represent the 1:1 lines for visual aid.

between the $\sigma_{\rm blue}$ measurements and two significant outliers for $\sigma_{\rm red}$ measurements. The first outlier is BAT 197 (HE 0351 +0240) which shows ≈ 0.1 dex difference in $\sigma_{\rm red}$ measurements, whereas its $\sigma_{\rm blue}$ measurements are essentially indistinguishable from each other (a difference of order 0.01 dex). The second outlier is BAT 562 (NGC 3822), which shows an offset of 0.09 dex in $\sigma_{\rm blue}$ and 0.11 dex in $\sigma_{\rm red}$ measurements. Such differences between $\sigma_\star$ measurements may be caused by systematic uncertainties in some cases, including varying observational conditions, instrumental resolutions and/or aperture sizes, and the detailed spectral features of the templates used, in the spectral regions of choice. Such systematic uncertainties can be as large as the statistical uncertainties obtained from the pPXF resampling approach. A detailed explanation of the systematic uncertainties is given by Koss et al. (2022b). At any rate, Figure 8 demonstrates the robustness of our methodology and—given the potential uncertainties and caveats—is an encouraging result.

Appendix C
Conversion between $\log(L_{14-150\,\rm keV}^{\rm int}/{\rm erg\ s^{-1}})$ and $\log(L_{14-195\,\rm keV}^{\rm obs}/{\rm erg\ s^{-1}})$

To measure $\log(L_{14-150\,\rm keV}^{\rm int}/{\rm erg\ s^{-1}})$ for our bonus sample of 55 AGNs, we first fit an orthogonal linear fit between $\log(L_{14-150\,\rm keV}^{\rm int}/{\rm erg\ s^{-1}})$ and $\log(L_{14-195\,\rm keV}^{\rm obs}/{\rm erg\ s^{-1}})$ for our sample of AGNs from the BAT 70 month catalog. Correspondingly, the resulting fit is found as follows:

$$\log(L_{14-150\,\rm keV}^{\rm int}/10^{44}) = \log(L_{14-195\,\rm keV}^{\rm obs}/10^{44})$$
$$- 0.06 \pm 0.01 \quad {\rm erg\ s^{-1}}. \qquad (C1)$$

The resulting intrinsic scatter (ϵ) of 0.09 ± 0.03 dex allows us to perform such a conversion confidently. Here, we note that we normalized the X-ray luminosities with the value of 10^{44} and also fixed the slope to 1 in order to avoid the correlation between the slope and intercept. In Figure 9, we present the conversation together with fitting results.
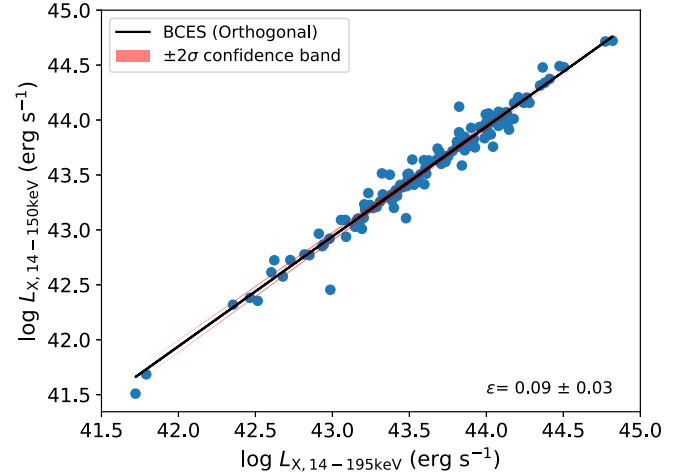

Figure 9. The fitting results for the conversion between $\log(L_{14-150\,\rm keV}^{\rm int}/{\rm erg\ s^{-1}})$ and $\log(L_{14-195\,\rm keV}^{\rm obs}/{\rm erg\ s^{-1}})$.

Appendix D
Comparison of Extinction-corrected and Uncorrected Black Hole Masses

Here, we note that the extinction in the BLR becomes somewhat important beyond $A_{\rm V} \simeq 1$. However, we stress that the majority of our sample (108 out of 165) have $A_{\rm V} < 1$. We also stress that the median difference between extinction-uncorrected and extinction-corrected $M_{\rm BH}$ is found to be 0.088 dex for our sample of AGNs. In only 32 cases, the difference exceeds 0.3 dex, and only six of them exceed 0.5 dex difference.

Appendix E
The Success Rate of $\sigma_\star$ Measurements and Various AGN Properties

In Figure 10, we present the distributions of several key properties for our AGN sample, split into successful and failed $\sigma_\star$ measurements, and for both $\sigma_{\rm blue}$ and $\sigma_{\rm red}$ measurements. We can see that the chance of obtaining successful $\sigma_\star$ fittings decreases with increasing redshift (top panels) and/or with
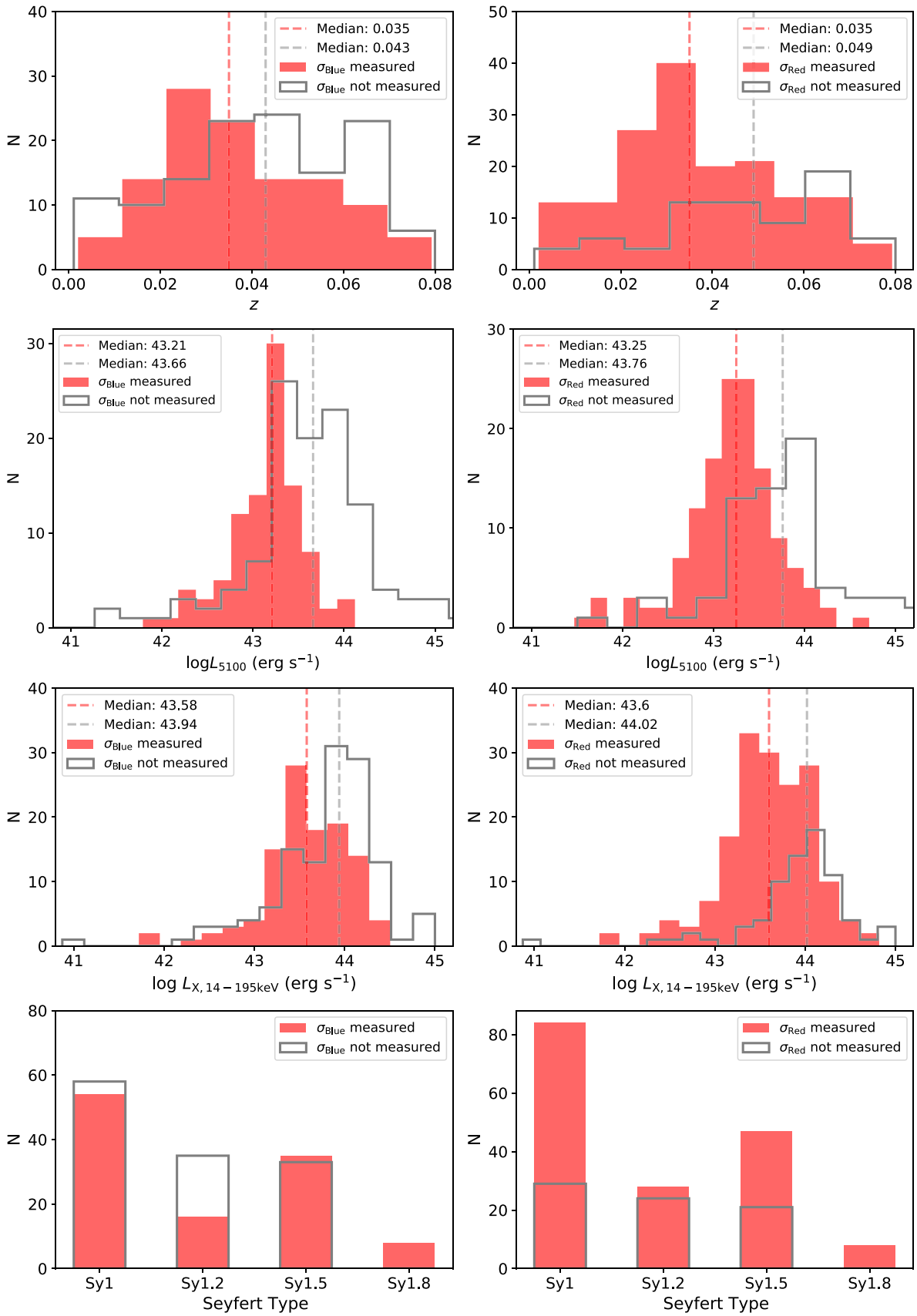
Figure 10. The distributions of successful vs. failed $\sigma_\star$ measurements with various AGN properties, for both $\sigma_{\rm blue}$ (left column) and $\sigma_{\rm red}$ (right column). From top to bottom, we show distributions of redshift z, optical continuum luminosity L_{5100}, ultra-hard X-ray luminosity $L_{\rm X,14-195\ keV}$, and Seyfert subtype.

increasing luminosity (either optical or ultra-hard X-rays; second and third-row panels, respectively). The latter could be caused by either stronger continuum emission or broad-line emission, both of which may dilute the stellar features. This might be considered a bias as the failed velocity dispersion objects tend to be the more luminous AGNs. Finally, we see no significant link between our ability to measure $\sigma_\star$ and the Seyfert subtypes (bottom panels of Figure 10).

Appendix F
The $M_{\mathrm{BH}}-\sigma_\star$ Relation for Various Data Sets

In Figure 11, we present the four different data sets considered for our BASS-based $M_{\mathrm{BH}}-\sigma_\star$ relations, and the corresponding best fits. The data sets are: all sources, with extinction-uncorrected measurements (DS1); sources with no signs of extinction ($A_\mathrm{V} = 0$; DS2); sources with some, but not extreme, extinction ($A_\mathrm{V} < 1$; DS3); and all sources, but using extinction-corrected measurements (DS4). The resulting fits are shown with $\pm 2\sigma$ confidence bands. Here, we remind the reader

that NGC 7213 was excluded from our data sets due to the unreliable M_{BH} measurement.

Appendix G
Galaxy Morphology and Aperture Corrections

Various spectral observables and derived parameters for galaxy centers are known to depend on the aperture used during observations (e.g., Jorgensen et al. 1995; Mehlert et al. 2003; Cappellari et al. 2006; Falcón-Barroso et al. 2017). This is particularly relevant for our work since galaxies generally have radial gradients in $\sigma_\star$ and in radial velocity. To investigate the importance of aperture effects and corrections for our analysis, we parameterize the $\sigma_\star$ gradient as a power law, that is,

$$\frac{\sigma_\mathrm{ap}}{\sigma_\mathrm{e}} = \left(\frac{r_\mathrm{ap}}{r_\mathrm{e}} \right)^{\alpha}, \qquad (G1)$$

where α is the slope of the gradient, r_e is the effective radius, r_ap is the aperture radius adopted in our spectroscopic observations, σ_ap is the $\sigma_\star$ we measure from these observations (at r_ap), and σ_e is the stellar velocity dispersion at r_e.
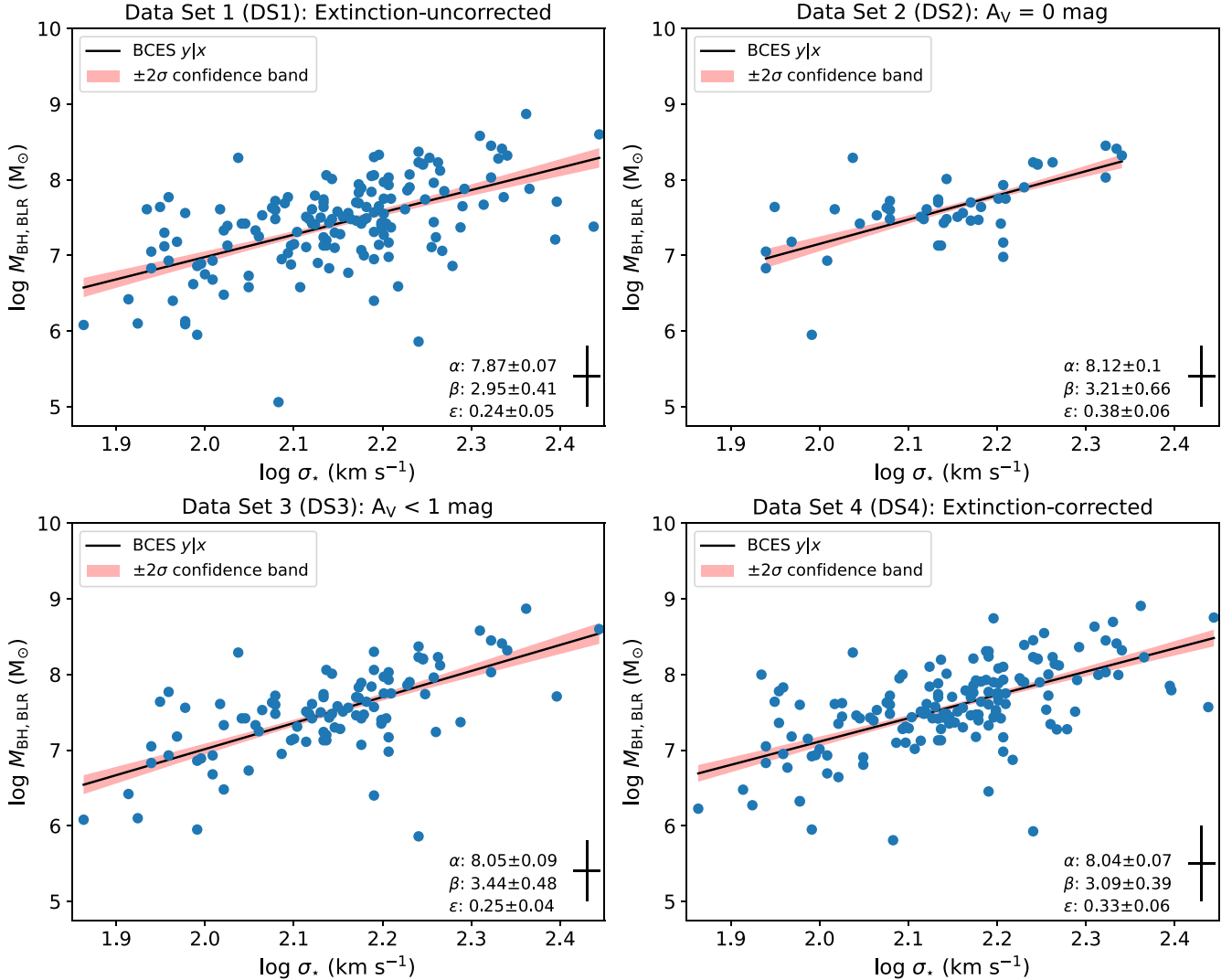

Figure 11. The $M_{\mathrm{BH}}-\sigma_\star$ relation of for different subsamples in our sample: DS1 (top left), DS2 (top right), DS3 (bottom right), and DS4 (bottom right). The fitting parameters are as follows: α is the intercept, β is the slope and ϵ is the intrinsic scatter of the $M_{\mathrm{BH}}-\sigma_\star$ relation. We show the median uncertainty in $\sigma_\star$ and M_{BH} as a black plus sign for visual aid.
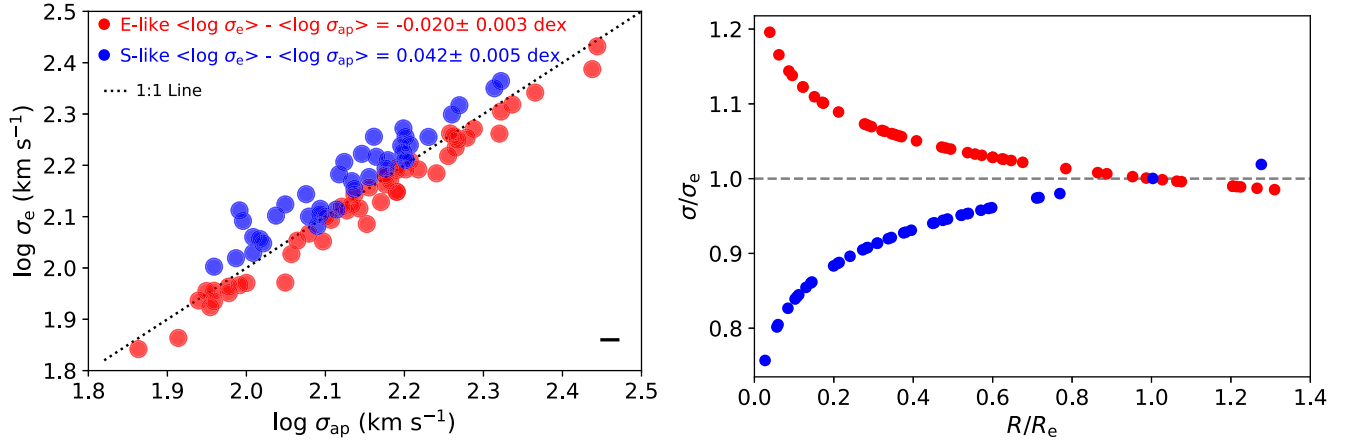
Figure 12. Left: comparison between the $\sigma_\star$ measurements obtained from our instruments' aperture sizes and effective radii. The black horizontal line represents the median uncertainty in $\sigma_\star$, whereas the black dotted line represents 1:1 line. Right: the normalized $\sigma_\star$ profiles integrated within elliptical apertures with increasing semimajor radius.

A further complication arises from the finding that the slopes of such $\sigma_\star$ gradients depend on the galaxy morphologies (and stellar masses for spiral galaxies, Falcón-Barroso et al. 2017). To incorporate this dependence, we collected the morphological classifications available for our sample galaxies from the literature (de Vaucouleurs et al. 1995; Vitores et al. 1996; Paturel et al. 2003; Deo et al. 2006; Nair & Abraham 2010; de Lapparent et al. 2011; Lintott et al. 2011), and divide them into two categories, essentially split into early-type (E-like) and late-type (S-like) objects. Considering the average stellar masses of BAT AGN hosts ($\log(M_\star/M_\odot) = 10.28 \pm 0.4$; Koss et al. 2011), we adopt $\alpha = -0.055$ for early-type (E+L) galaxies and $\alpha = 0.077$ for late-type (S), following (Falcón-Barroso et al. 2017). Finally, we collected K-band effective radii from the Two Micron All Sky Survey (Skrutskie et al. 2006) to compute the correction factor mentioned above.

In Figure 12, we demonstrate a direct comparison between the $\sigma_\star$ measurements obtained from our observations (i.e., instrumental apertures) and those expected at the effective radii. We find an average offset of -0.020 ± 0.003 dex between σ_e and σ_{ap} for E-like galaxies, and 0.042 ± 0.005 dex for S-like galaxies. The median relative error for our $\sigma_\star$ measurements (≈ 0.02 dex; see Section 4.1.1) is thus comparable to the offset caused by aperture effects. Aperture effects are thus unlikely to lead to large systematic errors in $\sigma_\star$, but they should be considered as part of the total $\sigma_\star$ error budget.

Appendix H
Spearman Rank-order Correlation Results

In Table 4, we present the results of the Spearman rank-order correlation tests we have conducted to look for links between various properties and parameters. The table is presented with color codes of p-values for visual aid.

Table 4
Spearman Rank-order Correlation Results

	$\sigma_\star$	$(1+z)$	FWHM$_{H\beta}$	$L_{H\beta}$	L_{5100}	$M_{BH,H\beta}$	FWHM$_{H\alpha}$	$L_{H\alpha}$	$M_{BH,H\alpha}$	N_H	L_{bol}	$\log \lambda_{Edd}$	A_V	$\Delta \mathcal{M}_{BH}$
$\sigma_\star$	1	0.36	0.51	0.27	0.31	0.55	0.48	0.33	0.51	−0.12	0.47	−0.21	0.09	−0.28
$\log(1+z)$	0.36	1	0.24	0.51	0.54	0.48	0.27	0.66	0.57	−0.01	0.83	0.06	0.01	0.33
FWHM$_{H\beta}$	0.51	0.24	1	−0.01	0.09	0.78	0.68	0.03	0.48	−0.02	0.24	−0.43	0.26	0.08
$L_{H\beta}$	0.27	0.51	−0.01	1	0.88	0.56	0.24	0.85	0.64	−0.06	0.6	−0.24	−0.49	0.42
L_{5100}	0.31	0.54	0.09	0.88	1	0.59	0.23	0.78	0.59	−0.07	0.55	−0.22	−0.43	0.33
$M_{BH,H\beta}$	0.55	0.48	0.78	0.56	0.59	1	0.68	0.52	0.78	−0.1	0.53	−0.49	−0.09	0.31
FWHM$_{H\alpha}$	0.48	0.27	0.68	0.24	0.23	0.68	1	0.23	0.79	−0.04	0.34	−0.72	0.09	0.39
$L_{H\alpha}$	0.33	0.66	0.03	0.85	0.78	0.52	0.23	1	0.74	−0.04	0.76	−0.18	−0.5	0.46
$M_{BH,H\alpha}$	0.51	0.57	0.48	0.64	0.59	0.78	0.79	0.74	1	−0.05	0.66	−0.59	−0.29	0.55
N_H	−0.12	−0.01	−0.02	−0.06	−0.07	−0.1	−0.04	−0.04	−0.05	1	0.01	0.09	0.05	0
A_V	0.47	0.83	0.24	0.6	0.55	0.53	0.34	0.76	0.66	0.01	1	0.09	0.06	0.27
L_{bol}	−0.21	0.06	−0.43	−0.24	−0.22	−0.49	−0.72	−0.18	−0.59	0.09	0.09	1	0.42	−0.47
$\log \lambda_{Edd}$	0.09	0.01	0.26	−0.49	−0.43	−0.09	0.09	−0.5	−0.29	0.05	0.06	0.42	1	−0.38
$\Delta \mathcal{M}_{BH}$	−0.28	0.33	0.08	0.42	0.33	0.31	0.39	0.46	0.55	0	0.27	−0.47	−0.38	1

Note. The table is presented with a color code of ρ values for visual aid. Black, blue, and red colors correspond to p-value $\leqslant 0.01$, p-value $\leqslant 0.05$, and p-value > 0.05, respectively.

Appendix I
PCA

To identify the main parameters that are driving the variance in our data set, we conduct a PCA focusing on the observable parameters as follows: $\sigma_\star$, $\log(1 + z)$, $FWHM_{H\alpha}$, $\log L_{H\alpha}$, A_V, and L_{bol}. Interestingly, the first three eigenvectors (EV 1, and EV 2) explain the 83.3% variance in the data set. The most dominant one is the first eigenvector, which explains the 48.6% variance. The remaining three eigenvectors explain 8.5%, 6.1%, and 2.1% variances, respectively. By inspecting the correlations of these eigenvectors with the selected variables (see Table 5), we find that the first and second eigenvectors are mostly driven by the anticorrelation between A_V and $L_{H\alpha}$ indicating an obscuration effect in the observed $L_{H\alpha}$, in agreement with previous works (C20; Mejía-Restrepo et al. 2022; Ricci et al. 2022). The correlations between z, luminosity (L_{bol}), and $\sigma_\star$ mostly drive the third eigenvector. This traces the selection bias resulting from the flux-limited nature of the sample, which favors the detection of high luminosity and high $\sigma_\star$ objects at higher redshifts. The remaining eigenvectors only explain the 16.7% variance of the data set, and there are at least four dominant parameters, which lay the responsibility for each eigenvector. This indicates a significant scatter in the measured properties suggesting that different parameters than the first, second, and third eigenvectors are the main drivers of the remaining eigenvectors.

Table 5
The Resulting Spearman Correlation Coefficients between the Select Features for Each Eigenvector (EV) from the PCA

Feature	EV 1	EV 2	EV 3	EV 4	EV 5	EV 6
Variance	48.6%	20.9%	13.8%	8.5%	6.1%	2.1%
$\log \sigma_\star$	0.22	−0.47	0.82	−0.19	0.19	−0.26
$\log(1 + z)$	−0.29	−0.02	0.79	0.03	0.09	−0.60
$\log FWHM_{H\alpha}$	0.39	−0.63	0.08	−0.17	0.74	−0.23
$\log L_{H\alpha}$	−0.79	0.66	0.53	0.06	0.31	−0.37
A_V	0.49	−0.81	0.21	−0.27	−0.39	−0.39
$\log L_{Bol}$	−0.43	0.15	0.74	0.03	0.36	−0.54

ORCID iDs

Turgay Caglar ● https://orcid.org/0000-0002-9144-2255
Michael J. Koss ● https://orcid.org/0000-0002-7998-9581
Leonard Burtscher ● https://orcid.org/0000-0003-1014-043X
Benny Trakhtenbrot ● https://orcid.org/0000-0002-3683-7297
M. Kiyami Erdim ● https://orcid.org/0000-0002-6770-5043
Julian E. Mejía-Restrepo ● https://orcid.org/0000-0001-8450-7463
Federica Ricci ● https://orcid.org/0000-0001-5742-5980
Meredith C. Powell ● https://orcid.org/0000-0003-2284-8603
Claudio Ricci ● https://orcid.org/0000-0001-5231-2645
Richard Mushotzky ● https://orcid.org/0000-0002-7962-5446
Franz E. Bauer ● https://orcid.org/0000-0002-8686-8737
Tonima T. Ananna ● https://orcid.org/0000-0001-8211-3807
Rudolf E. Bär ● https://orcid.org/0000-0001-5481-8607
Bernhard Brandl ● https://orcid.org/0000-0001-9737-169X
Jarle Brinchmann ● https://orcid.org/0000-0003-4359-8797
Fiona Harrison ● https://orcid.org/0000-0002-4226-8959
Kohei Ichikawa ● https://orcid.org/0000-0002-4377-903X
Darshan Kakkad ● https://orcid.org/0000-0002-2603-2639
Kyuseok Oh ● https://orcid.org/0000-0002-5037-951X
Rogério Riffel ● https://orcid.org/0000-0002-1321-1320
Lia F. Sartori ● https://orcid.org/0000-0001-8020-3884
Krista L. Smith ● https://orcid.org/0000-0001-5785-7038
Daniel Stern ● https://orcid.org/0000-0003-2686-9241
C. Megan Urry ● https://orcid.org/0000-0002-0745-9792

References

Akritas, M. G., & Bershady, M. A. 1996, ApJ, 470, 706
Almeida, A., Anderson, S. F., Argudo-Fernández, M., et al. 2023, ApJS, 267, 44
Ananna, T. T., Weigel, A. K., Trakhtenbrot, B., et al. 2022, ApJS, 261, 9
Baes, M., Buyle, P., Hau, G. K. T., & Dejonghe, H. 2003, MNRAS, 341, L44
Bandara, K., Crampton, D., & Simard, L. 2009, ApJ, 704, 1135
Batiste, M., Bentz, M. C., Raimundo, S. I., Vestergaard, M., & Onken, C. A. 2017, ApJL, 838, L10
Baumgartner, W. H., Tueller, J., Markwardt, C. B., et al. 2013, ApJS, 207, 19
Beifiori, A., Courteau, S., Corsini, E. M., & Zhu, Y. 2012, MNRAS, 419, 2497
Bellovary, J. M., Holley-Bockelmann, K., Gültekin, K., et al. 2014, MNRAS, 445, 2667
Bennert, V. N., Treu, T., Ding, X., et al. 2021, ApJ, 921, 36
Bentz, M. C., Cackett, E. M., Crenshaw, D. M., et al. 2016, ApJ, 830, 136
Bentz, M. C., Denney, K. D., Cackett, E. M., et al. 2006b, ApJ, 651, 775
Bentz, M. C., & Katz, S. 2015, PASP, 127, 67
Bentz, M. C., Peterson, B. M., Netzer, H., Pogge, R. W., & Vestergaard, M. 2009a, ApJ, 697, 160
Bentz, M. C., Peterson, B. M., Pogge, R. W., Vestergaard, M., & Onken, C. A. 2006a, ApJ, 644, 133
Bentz, M. C., Walsh, J. L., Barth, A. J., et al. 2009b, ApJ, 705, 199
Bernardi, M., Sheth, R. K., Tundo, E., & Hyde, J. B. 2007, ApJ, 660, 267
Bian, W.-H., & Zhao, Y.-H. 2003, PASJ, 55, 599
Blandford, R. D., & McKee, C. F. 1982, ApJ, 255, 419
Burtscher, L., Davies, R. I., Graciá-Carpio, J., et al. 2016, A&A, 586, A28
Caglar, T., Burtscher, L., Brandl, B., et al. 2020, A&A, 634, A114
Caglar, T., & Hudaverdi, M. 2017, MNRAS, 471, 4990
Cappellari, M. 2017, MNRAS, 466, 798
Cappellari, M. 2022, arXiv:2208.14974
Cappellari, M., Bacon, R., Bureau, M., et al. 2006, MNRAS, 366, 1126
Cappellari, M., & Emsellem, E. 2004, PASP, 116, 138
Cappellari, M., Scott, N., Alatalo, K., et al. 2013, MNRAS, 432, 1709
Chen, Y.-P., Trager, S. C., Peletier, R. F., et al. 2014, A&A, 565, A117
Collin, S., Kawaguchi, T., Peterson, B. M., & Vestergaard, M. 2006, A&A, 456, 75
Curran, P. A. 2014, arXiv:1411.3816
Dalla Bontà, E., Peterson, B. M., Bentz, M. C., et al. 2020, ApJ, 903, 112
Davies, R. I., Burtscher, L., Rosario, D., et al. 2015, ApJ, 806, 127
de Jong, R. S., Barden, S. C., Bellido-Tirado, O., et al. 2016, Proc. SPIE, 9908, 99081O
de Lapparent, V., Baillard, A., & Bertin, E. 2011, A&A, 532, A75
de Vaucouleurs, G., de Vaucouleurs, A., Corwin, H. G., et al. 1995, yCat, 7155, 0
Debattista, V. P., Kazantzidis, S., & van den Bosch, F. C. 2013, ApJ, 765, 23
Denney, K. D., Bentz, M. C., Peterson, B. M., et al. 2006, ApJ, 653, 152
Denney, K. D., Peterson, B. M., Pogge, R. W., et al. 2010, ApJ, 721, 715
Deo, R. P., Crenshaw, D. M., & Kraemer, S. B. 2006, AJ, 132, 321
Duras, F., Bongiorno, A., Ricci, F., et al. 2020, A&A, 636, A73
Eun, D.-i., Woo, J.-H., & Bae, H.-J. 2017, ApJ, 842, 5
Falcón-Barroso, J., Lyubenova, M., van de Ven, G., et al. 2017, A&A, 597, A48
Ferrarese, L. 2002, ApJ, 578, 90
Ferrarese, L., & Merritt, D. 2000, ApJL, 539, L9
Garcia-Rissmann, A., Vega, L. R., Asari, N. V., et al. 2005, MNRAS, 359, 765
Gebhardt, K., Bender, R., Bower, G., et al. 2000, ApJL, 539, L13
Gonneau, A., Lyubenova, M., Lançon, A., et al. 2020, A&A, 634, A133
Graham, A. W. 2008, ApJ, 680, 143
Graham, A. W., & Li, I. h. 2009, ApJ, 698, 812
Graham, A. W., Onken, C. A., Athanassoula, E., & Combes, F. 2011, MNRAS, 412, 2211
Greene, J. E., & Ho, L. C. 2005, ApJ, 630, 122
Greene, J. E., & Ho, L. C. 2006, ApJ, 641, 117
Greene, J. E., Peng, C. Y., Kim, M., et al. 2010, ApJ, 721, 26
Grier, C. J., Martini, P., Watson, L. C., et al. 2013, ApJ, 773, 90
Grier, C. J., Pancoast, A., Barth, A. J., et al. 2017, ApJ, 849, 146
Gültekin, K., Richstone, D. O., Gebhardt, K., et al. 2009, ApJ, 698, 198

Häring, N., & Rix, H.-W. 2004, ApJL, 604, L89
Hartmann, M., Debattista, V. P., Cole, D. R., et al. 2014, MNRAS, 441, 1243
Ho, L. C. 2005, ApJ, 629, 680
Ho, L. C., Greene, J. E., Filippenko, A. V., & Sargent, W. L. W. 2009, ApJS, 183, 1
Ho, L. C., & Kim, M. 2014, ApJ, 789, 17
Hu, J. 2008, MNRAS, 386, 2242
Ichikawa, K., Ricci, C., Ueda, Y., et al. 2017, ApJ, 835, 74
Ichikawa, K., Ricci, C., Ueda, Y., et al. 2019, ApJ, 870, 31
Jorgensen, I., Franx, M., & Kjaergaard, P. 1995, MNRAS, 276, 1341
Kang, W.-R., Woo, J.-H., Schulze, A., et al. 2013, ApJ, 767, 26
Kaspi, S., Maoz, D., Netzer, H., et al. 2005, ApJ, 629, 61
Kaspi, S., Smith, P. S., Netzer, H., et al. 2000, ApJ, 533, 631
Kim, M., Ho, L. C., & Im, M. 2006, ApJ, 642, 702
King, A. 2003, ApJL, 596, L27
Kollmeier, J. A., Zasowski, G., Rix, H.-W., et al. 2017, arXiv:1711.03234
Koratkar, A. P., & Gaskell, C. M. 1991, ApJL, 370, L61
Kormendy, J., & Ho, L. C. 2013, ARA&A, 51, 511
Kormendy, J., & Kennicutt, R. C. J. 2004, ARA&A, 42, 603
Kormendy, J., & Richstone, D. 1995, ARA&A, 33, 581
Koss, M., Mushotzky, R., Veilleux, S., et al. 2011, ApJ, 739, 57
Koss, M., Trakhtenbrot, B., Ricci, C., et al. 2017, ApJ, 850, 74
Koss, M. J., Assef, R., Baloković, M., et al. 2016, ApJ, 825, 85
Koss, M. J., Ricci, C., Trakhtenbrot, B., et al. 2022c, ApJS, 261, 2
Koss, M. J., Strittmatter, B., Lamperti, I., et al. 2021, ApJS, 252, 29
Koss, M. J., Trakhtenbrot, B., Ricci, C., et al. 2022a, ApJS, 261, 1
Koss, M. J., Trakhtenbrot, B., Ricci, C., et al. 2022b, ApJS, 261, 6
Lauer, T. R., Tremaine, S., Richstone, D., & Faber, S. M. 2007, ApJ, 670, 249
Lintott, C., Schawinski, K., Bamford, S., et al. 2011, MNRAS, 410, 166
Lira, P., Kaspi, S., Netzer, H., et al. 2018, ApJ, 865, 56
Magorrian, J., Tremaine, S., Richstone, D., et al. 1998, AJ, 115, 2285
Marasco, A., Cresci, G., Posti, L., et al. 2021, MNRAS, 507, 4274
Marconi, A., & Hunt, L. K. 2003, ApJL, 589, L21
Marconi, A., Risaliti, G., Gilli, R., et al. 2004, MNRAS, 351, 169
Marinucci, A., Bianchi, S., Nicastro, F., Matt, G., & Goulding, A. D. 2012, ApJ, 748, 130
Martini, P., & Weinberg, D. H. 2001, ApJ, 547, 12
McConnell, N. J., & Ma, C.-P. 2013, ApJ, 764, 184
Mehlert, D., Thomas, D., Saglia, R. P., Bender, R., & Wegner, G. 2003, A&A, 407, 423
Mejía-Restrepo, J. E., Lira, P., Netzer, H., Trakhtenbrot, B., & Capellupo, D. M. 2018a, NatAs, 2, 63
Mejía-Restrepo, J. E., Trakhtenbrot, B., Koss, M. J., et al. 2022, ApJS, 261, 5
Mejía-Restrepo, J. E., Trakhtenbrot, B., Lira, P., & Netzer, H. 2018b, MNRAS, 478, 1929
Mejía-Restrepo, J. E., Trakhtenbrot, B., Lira, P., Netzer, H., & Capellupo, D. M. 2016, MNRAS, 460, 187
Merritt, D., & Ferrarese, L. 2001, ApJ, 547, 140
Mondal, S., Adhikari, T. P., Hryniewicz, K., Stalin, C. S., & Pandey, A. 2022, A&A, 662, A77
Mushotzky, R. 2018, Proc. SPIE, 10699, 1069929
Nair, P. B., & Abraham, R. G. 2010, ApJS, 186, 427
Nandra, K., Barret, D., Barcons, X., et al. 2013, arXiv:1306.2307
Nelson, C. H., Green, R. F., Bower, G., Gebhardt, K., & Weistrop, D. 2004, ApJ, 615, 652
Nelson, C. H., & Whittle, M. 1995, ApJS, 99, 67
Nemmen, R. S., Georganopoulos, M., Guiriec, S., et al. 2012, Sci, 338, 1445
Nowak, M. A., Neilsen, J., Markoff, S. B., et al. 2012, ApJ, 759, 95
Oh, K., Koss, M., Markwardt, C. B., et al. 2018, ApJS, 235, 4
Oh, K., Koss, M. J., Ueda, Y., et al. 2022, ApJS, 261, 4
Oliva, E., Origlia, L., Kotilainen, J. K., & Moorwood, A. F. M. 1995, A&A, 301, 55
Oliva, E., Origlia, L., Maiolino, R., & Moorwood, A. F. M. 1999, A&A, 350, 9
Onken, C. A., Ferrarese, L., Merritt, D., et al. 2004, ApJ, 615, 645
Onken, C. A., & Peterson, B. M. 2002, ApJ, 572, 746

Pancoast, A., Brewer, B. J., Treu, T., et al. 2014, MNRAS, 445, 3073
Park, D., Barth, A. J., Woo, J.-H., et al. 2017, ApJ, 839, 93
Park, D., Kelly, B. C., Woo, J.-H., & Treu, T. 2012, ApJS, 203, 6
Paturel, G., Petit, C., Prugniel, P., et al. 2003, A&A, 412, 45
Peterson, B. M. 1993, PASP, 105, 247
Peterson, B. M., Ferrarese, L., Gilbert, K. M., et al. 2004, ApJ, 613, 682
Powell, M. C., Allen, S. W., Caglar, T., et al. 2022, ApJ, 938, 77
Predehl, P., Andritschke, R., Arefiev, V., et al. 2021, A&A, 647, A1
Predehl, P., & Schmitt, J. H. M. M. 1995, A&A, 500, 459
Proga, D., & Kallman, T. R. 2004, ApJ, 616, 688
Ricarte, A., Tremmel, M., Natarajan, P., & Quinn, T. 2019, MNRAS, 489, 802
Ricci, C., Ananna, T. T., Temple, M. J., et al. 2022, ApJ, 938, 67
Ricci, C., & Trakhtenbrot, B. 2022, arXiv:2211.05132
Ricci, C., Trakhtenbrot, B., Koss, M. J., et al. 2017a, Natur, 549, 488
Ricci, C., Trakhtenbrot, B., Koss, M. J., et al. 2017b, ApJS, 233, 17
Ricci, C., Ueda, Y., Koss, M. J., et al. 2015, ApJL, 815, L13
Ricci, F., La Franca, F., Onori, F., & Bianchi, S. 2017c, A&A, 598, A51
Ricci, F., Treister, E., Bauer, F. E., et al. 2022, ApJS, 261, 8
Riffel, R. A., Ho, L. C., Mason, R., et al. 2015, MNRAS, 446, 2823
Risaliti, G., Maiolino, R., & Bassani, L. 2000, A&A, 356, 33
Risaliti, G., Salvati, M., Elvis, M., et al. 2009, MNRAS Lett., 393, L1
Sabra, B. M., Saliba, C., Abi Akl, M., & Chahine, G. 2015, ApJ, 803, 5
Saglia, R. P., Opitsch, M., Erwin, P., et al. 2016, ApJ, 818, 47
Schawinski, K., Koss, M., Berney, S., & Sartori, L. F. 2015, MNRAS, 451, 2517
Schnorr-Müller, A., Davies, R. I., Korista, K. T., et al. 2016, MNRAS, 462, 3570
Shankar, F., Bernardi, M., Sheth, R. K., et al. 2016, MNRAS, 460, 3119
Shen, Y. 2013, BASI, 41, 61
Shen, Y. 2021, ApJ, 921, 70
Shen, Y., Greene, J. E., Ho, L. C., et al. 2015, ApJ, 805, 96
Shen, Y., Greene, J. E., Strauss, M. A., Richards, G. T., & Schneider, D. P. 2008, ApJ, 680, 169
Shen, Y., Horne, K., Grier, C. J., et al. 2016, ApJ, 818, 30
Shen, Y., & Liu, X. 2012, ApJ, 753, 125
Shimizu, T. T., Davies, R. I., Koss, M., et al. 2018, ApJ, 856, 154
Shimizu, T. T., Mushotzky, R. F., Meléndez, M., Koss, M., & Rosario, D. J. 2015, MNRAS, 452, 1841
Silk, J., & Rees, M. J. 1998, A&A, 331, L1
Skrutskie, M. F., Cutri, R. M., Stiening, R., et al. 2006, AJ, 131, 1163
Soltan, A. 1982, MNRAS, 200, 115
Storchi-Bergmann, T., Schimoia, J. S., Peterson, B. M., et al. 2017, ApJ, 835, 236
Temple, M. J., Ricci, C., Koss, M. J., et al. 2022, MNRAS, 518, 2938
Terlevich, E., Diaz, A. I., & Terlevich, R. 1990, MNRAS, 242, 271
Trakhtenbrot, B., & Netzer, H. 2012, MNRAS, 427, 3081
Tremaine, S., Gebhardt, K., Bender, R., et al. 2002, ApJ, 574, 740
van den Bosch, R. C. E. 2016, ApJ, 831, 134
van den Bosch, R. C. E., Gebhardt, K., Gültekin, K., Yıldırım, A., & Walsh, J. L. 2015, ApJS, 218, 10
Vasudevan, R. V., Mushotzky, R. F., Winter, L. M., & Fabian, A. C. 2009, MNRAS, 399, 1553
Villafaña, L., Williams, P. R., Treu, T., et al. 2022, ApJ, 930, 52
Vitores, A. G., Zamorano, J., Rego, M., Alonso, O., & Gallego, J. 1996, A&AS, 118, 7
Volonteri, M. 2012, Sci, 337, 544
Volonteri, M., Natarajan, P., & Gültekin, K. 2011, ApJ, 737, 50
Walton, D. J., Risaliti, G., Harrison, F. A., et al. 2014, ApJ, 788, 76
Wegner, G., Bernardi, M., Willmer, C. N. A., et al. 2003, AJ, 126, 2268
Wild, V., Charlot, S., Brinchmann, J., et al. 2011, MNRAS, 417, 1760
Woo, J.-H., Schulze, A., Park, D., et al. 2013, ApJ, 772, 49
Woo, J.-H., Treu, T., Barth, A. J., et al. 2010, ApJ, 716, 269
Woo, J.-H., Yoon, Y., Park, S., Park, D., & Kim, S. C. 2015, ApJ, 801, 38
Xiao, T., Barth, A. J., Greene, J. E., et al. 2011, ApJ, 739, 28
Yuan, F., Lidman, C., Davis, T. M., et al. 2015, MNRAS, 452, 3047
Zajaček, M., Czerny, B., Martinez-Aldama, M. L., et al. 2020, ApJ, 896, 146